




Fast Voxelwise SNR Estimation for Iterative MRI Reconstructions

Onat Dalmaz ^{1,2}, Daniel Abraham ^{1,2}, Alexander R. Toews ^{1,2}, Akshay S. Chaudhari ^{2,4},
Kawin Setsompop ^{1,2}, and Brian A. Hargreaves ^{1,2,3}

¹*Department of Electrical Engineering, Stanford University, California, USA*

²*Department of Radiology, Stanford University, California, USA*

³*Department of Bioengineering, Stanford University, California, USA*

⁴*Department of Biomedical Data Science, Stanford University, California, USA*

Correspondence: onat@stanford.edu

May 12, 2026

Abstract

Purpose. To develop a fast, general-purpose framework for voxelwise noise characterization in MRI reconstructions, applicable to both linear and nonlinear iterative reconstructions. The framework recovers the voxelwise image-domain noise variance—the primary quantity from which signal-to-noise ratio (SNR), g -factor, and related image-quality metrics are derived—addressing both the computational intractability of closed-form formulas beyond Cartesian sampling and the excessive runtime of empirical Pseudo Multiple Replica (PMR) methods.

Methods. A novel noise estimator—which we term PICO (Probing Image-space COvariance)—is proposed that operates entirely in the image domain by probing the image-domain noise covariance operator—or, for nonlinear compressed-sensing reconstructions, the Jacobian of the converged solution—with random probe images. Complex random-phase probes are shown theoretically and empirically to minimize estimator variance compared with Gaussian or real-valued alternatives. The method was validated against analytical benchmarks and high-replica PMR references using retrospective Cartesian knee data ($R = 2$), prospective non-Cartesian spiral brain phantom data ($R = 2, 3, 4$), and compressed-sensing knee reconstructions ($R = 2$).

Results. In Cartesian experiments, PICO accurately reproduced analytical SENSE g -factor maps. In non-Cartesian spiral imaging ($R = 2$), it achieved 1% estimation error in 64 s compared with 462 s for PMR ($\approx 7.2\times$ speedup), with the efficiency advantage persisting at higher acceleration factors. For nonlinear compressed sensing, the Jacobian-based estimator produced noise maps consistent with PMR while converging faster (52 s vs. 95 s; $\approx 1.8\times$ speedup).

Conclusion. The proposed stochastic framework provides a computationally efficient alternative to PMR for voxelwise noise and g -factor estimation, enabling rapid SNR characterization for generalized MRI reconstructions—including non-Cartesian, regularized, and nonlinear pipelines—where closed-form noise analysis is otherwise unavailable. By reusing existing reconstruction primitives, the method enables voxelwise noise maps to be produced as a routine by-product of the reconstruction pipeline itself.

Keywords: noise estimation; SNR; parallel imaging; CG-SENSE; iterative reconstructions; compressed sensing; g -factor; non-Cartesian MRI.

1 Introduction

Signal-to-noise ratio (SNR) is a fundamental measure of image quality in MRI [1–3]. Every reconstructed image—whether from a fully sampled single-coil acquisition, a multi-coil parallel imaging scan, or a heavily accelerated compressed-sensing protocol—carries noise whose spatial structure and local magnitude determines the reliability of each voxel for diagnosis, quantification, and downstream analysis [4, 5]. Voxelwise noise variance maps provide the most complete characterization of this variability: global summary metrics such as mean SNR or contrast-to-noise ratio can mask significant local noise amplification that impedes detection of subtle pathologies, even when aggregate quality appears acceptable [6, 7]. Accurate voxelwise noise maps are therefore essential for quality assurance, protocol optimization, comparison of reconstruction strategies, and principled selection of regularization parameters [5, 8–10].

During the foundational era of parallel imaging, noise analysis was tightly integrated with reconstruction development. Pruessmann et al. derived a closed-form geometry factor (g -factor) alongside the original SENSE formulation [11], providing not only an analytical voxelwise noise amplification map for uniformly sampled Cartesian acquisitions but also the conceptual framework through which voxelwise SNR has been quantified in parallel imaging ever since. Analogous expressions were developed for SMASH [12] and GRAPPA [13], and Kellman and McVeigh showed that images could be reconstructed directly in SNR units using pre-scan noise calibration [5]. These tools were instrumental in algorithm design and clinical validation [14, 15]. As reconstruction pipelines have grown more complex—moving from direct-inversion Cartesian methods to iterative solvers for non-Cartesian trajectories [16–18], compressed sensing with non-smooth regularizers [19, 20], and deep-learning-based pipelines [21, 22]—the encoding operators (NUFFT, gridding, variable-density compensation) have become difficult to form or invert at scale [16, 23, 24], and the closed-form formulas that once made noise characterization routine are simply inapplicable. As a result, much of the reconstruction literature over the past two decades has either omitted noise analysis entirely or relegated it to post hoc characterization, decoupled from reconstruction development [25, 26].

In the absence of closed-form noise expressions for these modern reconstruction pipelines, the principal alternative has been the Pseudo Multiple Replica (PMR) method [27], which treats the reconstruction as an opaque black box: synthetic noise is injected into k -space, a full reconstruction is re-run for each replica, and voxelwise variance is estimated from the image ensemble. For computationally intensive reconstructions—such as non-Cartesian iterative methods, Tikhonov-regularized CG-SENSE, and compressed sensing solvers—this requires a complete iterative solve per replica [25, 28, 29]. Beyond the computational cost of repeating the full solve for every replica [25, 28, 29], PMR is fundamentally limited by statistical inefficiency. Because it discards all structural knowledge of the reconstruction operator—in particular, known factorizations of the covariance matrix—PMR estimates variance from squared magnitudes of complex-Gaussian outputs, whose heavy-tailed (sub-exponential) distribution causes disproportionately slow convergence in high-noise-amplification regions where accurate characterization matters most (Appendix C). The resulting wall-clock times have limited PMR adoption in practice and prevented its integration into real-time or inline workflows [26, 27, 30]. To reduce computational cost, Wiens et al. proposed a generalized pseudo-replica method that replaces the N -replica ensemble with a *spatial* average: a single noise-injected reconstruction is differenced against an unperturbed reference, and voxelwise variance is estimated from the standard deviation of the difference image within a sliding local window [31]. This delivers a sizable speedup over PMR but introduces three structural limitations. First, the estimator is fundamentally approximate: at every voxel k , it converges not to the true voxelwise variance $(\Sigma_{\mathbf{x}})_{kk}$ but to a local spatial average over the window, so the resulting noise

map is inherently smoothed and biased wherever the g-factor varies within the averaging volume—precisely the high-g-factor boundaries where accurate characterization matters most. Second, the pointwise squared-deviation samples remain sub-exponential, so spatial averaging inherits the same heavy-tailed per-sample variance that governs PMR (Appendix C); the method trades temporal replicas for spatial neighbors without escaping the underlying statistical inefficiency. Third, the subtraction step relies on a linearity argument that does not extend to non-smooth regularizers such as total variation or ℓ_1 , confining the method to linear reconstructions. The generalized pseudo-replica method therefore reduces the replica count at the cost of a structurally biased, resolution-limited estimator confined to linear pipelines, without exploiting any knowledge of the reconstruction operator.

Recent work has begun to address noise estimation in deep-learning-based reconstructions by locally linearizing the converged reconstruction map and using automatic differentiation to form Jacobian–vector products. This approach has been applied to unrolled deep networks [32] and to k -space interpolation (RAKI) networks [33, 34], representing important progress toward tractable noise analysis for modern learned reconstructions. These methods, however, have three limitations that leave the broader problem unresolved. First, they are inherently approximate: the Jacobian captures only the first-order behavior of the reconstruction map at a single operating point, and the quality of the resulting variance estimate depends on how faithfully this linearization reflects the true nonlinear response. Second, they do not exploit the known structure of the encoding operator and its adjoint, treating the reconstruction as a generic differentiable map rather than as the solution of a specific physics-driven inverse problem. Third, and most importantly, they have not been developed for iterative linear reconstructions or for regularized compressed-sensing reconstructions—despite the fact that CG-SENSE and closely related linear iterative methods remain the most widely deployed reconstruction class in both clinical and research practice, and admit an *exact*, fully analytical characterization of the image-domain noise covariance. A framework that directly exploits this known structure—recovering the exact covariance for linear reconstructions while extending naturally to nonlinear ones—has so far been absent.

In this work, we invert the standard paradigm of MRI noise characterization. Rather than injecting synthetic noise into k -space and averaging over many full reconstructions, we leave the acquired data untouched and probe the image-domain noise-propagation operator directly with stochastic image-space probes—recovering voxelwise variance from how the operator responds, rather than from how reconstructions fluctuate. We call this framework PICO (Probing Image-space CO-variance). For linear reconstructions such as CG-SENSE with or without regularization—including the unaccelerated reference case that underlies essentially all quantitative SNR studies—PICO is mathematically exact: it recovers the diagonal of the noise covariance without any linearization, Jacobian approximation, or model simplification. The only source of error is finite-sample Monte Carlo variance, which decreases as $1/N$ and, unlike PMR’s heavy-tailed sub-exponential behavior, concentrates with sub-Gaussian tails whose decay rate is *independent* of the local noise amplitude (Appendix C). Empirically, this translates into a substantial efficiency advantage over PMR that is retained across acceleration factors: as the reconstruction becomes more ill-conditioned, PMR requires disproportionately more additional replicas to maintain a given accuracy than PICO requires additional probes, so PICO scales more gracefully in the regimes where accurate noise characterization is hardest. Crucially, PICO requires no new computational infrastructure: its implicit covariance–vector products reuse the exact CG-SENSE primitives already present in any iterative reconstruction pipeline—forward and adjoint operators, regularized normal-equation solves, NUFFT, Toeplitz embeddings, and any physics corrections (off-resonance, density compensation) the reconstruction supports.

The same framework extends cleanly to nonlinear reconstructions (e.g., compressed sensing

with total-variation or ℓ_1 regularization) by applying the estimator to a first-order Jacobian linearization of the converged reconstruction map via automatic-differentiation Jacobian–vector products, unifying the linear exact and nonlinear approximate regimes under a single algorithm. Crucially, the choice of probe distribution in both regimes is not a heuristic. Building on the classical stochastic diagonal estimators of Hutchinson and Bekas et al. [35, 36], we generalize the variance analysis from real symmetric to complex Hermitian positive-semidefinite operators and prove that *random-phase probes*—unit-magnitude complex vectors with uniformly distributed phase—attain the minimum achievable per-sample estimator variance among all unit-variance probe distributions, strictly outperforming both standard complex Gaussian and real-valued Rademacher alternatives (Appendix B). To our knowledge, this kurtosis-optimal probe structure has not previously been exploited for MRI noise characterization. Taken together, these contributions re-establish voxelwise SNR characterization as a lightweight, physics-grounded by-product of the reconstruction pipeline itself—available across a broad range of reconstruction types including direct-inversion Cartesian SENSE, iterative CG-SENSE on arbitrary trajectories, Tikhonov-regularized linear solvers, and nonlinear compressed-sensing reconstructions

To demonstrate PICO, we apply it to three representative MRI reconstruction settings. On retrospectively undersampled Cartesian knee data at $R = 2$, the estimator is compared against the closed-form analytical SENSE noise reference, providing a ground-truth benchmark where one exists. On prospective non-Cartesian spiral brain phantom data at $R \in \{2, 3, 4\}$, where no closed-form reference is available, we use a high-replica PMR estimate whose convergence is independently certified (Appendix E); benchmarking against PMR’s own converged output is deliberately conservative, since any residual PMR-specific bias is absorbed into the reference rather than penalized. On compressed-sensing reconstructions of the fastMRI knee dataset at $R = 2$, a total-variation–regularized FISTA pipeline exercises the Jacobian extension in a representative nonlinear setting. An ablation study empirically confirms the kurtosis-based probe-optimality theory, and a robustness study demonstrates that the Jacobian approximation remains accurate across the full range of SNRs encountered in standard acquisitions, with visible departures from PMR appearing only at stress-test noise levels where the underlying reconstruction itself becomes strongly nonlinear.

2 Theory

2.1 MRI Reconstruction and Noise

2.1.1 Acquisition Model

Let $\mathbf{x} \in \mathbb{C}^{N_x}$ be the image and $\mathbf{b} \in \mathbb{C}^{N_k}$ the stacked multi-coil k-space data. The generalized linear encoding operator $\tilde{\mathbf{A}} \in \mathbb{C}^{N_k \times N_x}$ includes coil sensitivities, Fourier/NUFFT, density compensation, and sampling trajectory:

$$\mathbf{b} = \tilde{\mathbf{A}}\mathbf{x} + \mathbf{n}. \quad (1)$$

2.1.2 Multi-Coil Noise and Pre-Whitening

Acquisition noise is modeled as circular complex Gaussian with multi-channel noise covariance matrix $\Sigma_{\mathbf{n}}$:

$$\mathbf{n} \sim \mathcal{CN}(\mathbf{0}, \Sigma_{\mathbf{n}}), \quad \Sigma_{\mathbf{n}} \succeq \mathbf{0}. \quad (2)$$

Let $\mathbf{L}\mathbf{L}^H = \Sigma_{\mathbf{n}}$ (e.g., Cholesky factorization). Left-multiplying (1) by \mathbf{L}^{-1} yields the pre-whitened system

$$\mathbf{b}_w = \mathbf{A}\mathbf{x} + \mathbf{n}_w, \quad \mathbf{A} = \mathbf{L}^{-1}\tilde{\mathbf{A}}, \quad \mathbf{n}_w = \mathbf{L}^{-1}\mathbf{n} \sim \mathcal{CN}(\mathbf{0}, \mathbf{I}). \quad (3)$$

All subsequent derivations and experiments operate on the pre-whitened system of Eq. (3). Pre-whitening is a standard first step in multi-coil reconstruction pipelines [27, 37]: it folds the inter-coil noise correlations into the encoding operator through \mathbf{L}^{-1} , leaving residual noise that is spatially white and unit-variance across channels. As a result, the image-domain noise covariance of any linear reconstruction depends only on the reconstruction operator \mathbf{R} acting on the pre-whitened data (Eq. (7)), and the proposed estimator probes $\Sigma_{\hat{\mathbf{x}}} = \mathbf{R}\mathbf{R}^H$ without requiring explicit knowledge of the original channel noise correlations.

2.1.3 Reconstruction model and operators: from least squares to CG-SENSE and beyond

In practice, pre-whitened multi-coil MRI data are modeled as $\mathbf{b}_w = \mathbf{A}\mathbf{x} + \mathbf{n}_w$ with $\mathbf{n}_w \sim \mathcal{CN}(\mathbf{0}, \mathbf{I})$. A standard workhorse in clinical and research pipelines is a quadratic (least-squares) objective with optional ℓ_2 (Tikhonov) stabilization:

$$\hat{\mathbf{x}}_\lambda \in \arg \min_{\mathbf{x}} \frac{1}{2} \|\mathbf{A}\mathbf{x} - \mathbf{b}_w\|_2^2 + \frac{\lambda}{2} \|\mathbf{x}\|_2^2, \quad \lambda \geq 0. \quad (4)$$

This objective is convex and *quadratic*; its minimizer depends *linearly* on the data. Equivalently, there exists a linear reconstruction operator \mathbf{R}_λ such that

$$\hat{\mathbf{x}}_\lambda = \mathbf{R}_\lambda \mathbf{b}_w, \quad \mathbf{R}_\lambda = (\mathbf{A}^H \mathbf{A} + \lambda \mathbf{I})^{-1} \mathbf{A}^H. \quad (5)$$

Forming $(\mathbf{A}^H \mathbf{A} + \lambda \mathbf{I})^{-1}$ explicitly is unnecessary in large-scale MRI [38]. Instead, one solves the normal equations

$$(\mathbf{A}^H \mathbf{A} + \lambda \mathbf{I}) \mathbf{x} = \mathbf{A}^H \mathbf{b}_w, \quad (6)$$

with conjugate gradients (CG). This is precisely the CG-SENSE procedure widely used in routine workflows: it exploits fast applications of \mathbf{A} and \mathbf{A}^H (FFT/NUFFT + sensitivity maps) and avoids matrix factorizations [16, 18].

2.1.4 Noise propagation and covariance

With pre-whitened noise $\mathbf{n}_w \sim \mathcal{CN}(\mathbf{0}, \mathbf{I})$ and the linear reconstruction $\hat{\mathbf{x}}_\lambda = \mathbf{R}_\lambda \mathbf{b}_w$ from Eq. (5), the image-domain noise *covariance* matrix (not correlation matrix—the diagonal entries give voxelwise noise variances, not unity) follows directly as

$$\Sigma_{\hat{\mathbf{x}}} = \text{Cov}[\hat{\mathbf{x}}_\lambda] = \mathbf{R}_\lambda \mathbf{R}_\lambda^H. \quad (7)$$

Substituting \mathbf{R}_λ yields the familiar expressions

$$\Sigma_{\hat{\mathbf{x}}} = (\mathbf{A}^H \mathbf{A} + \lambda \mathbf{I})^{-1} \mathbf{A}^H \mathbf{A} (\mathbf{A}^H \mathbf{A} + \lambda \mathbf{I})^{-1}, \quad \lambda \geq 0, \quad (8)$$

and, in the unregularized case ($\lambda = 0$) with invertible $\mathbf{A}^H \mathbf{A}$,

$$\Sigma_{\hat{\mathbf{x}}} = (\mathbf{A}^H \mathbf{A})^{-1}. \quad (9)$$

The voxelwise noise variance map is the diagonal [11, 13]

$$\sigma_{\hat{\mathbf{x}}}^2 = \text{diag}(\Sigma_{\hat{\mathbf{x}}}). \quad (10)$$

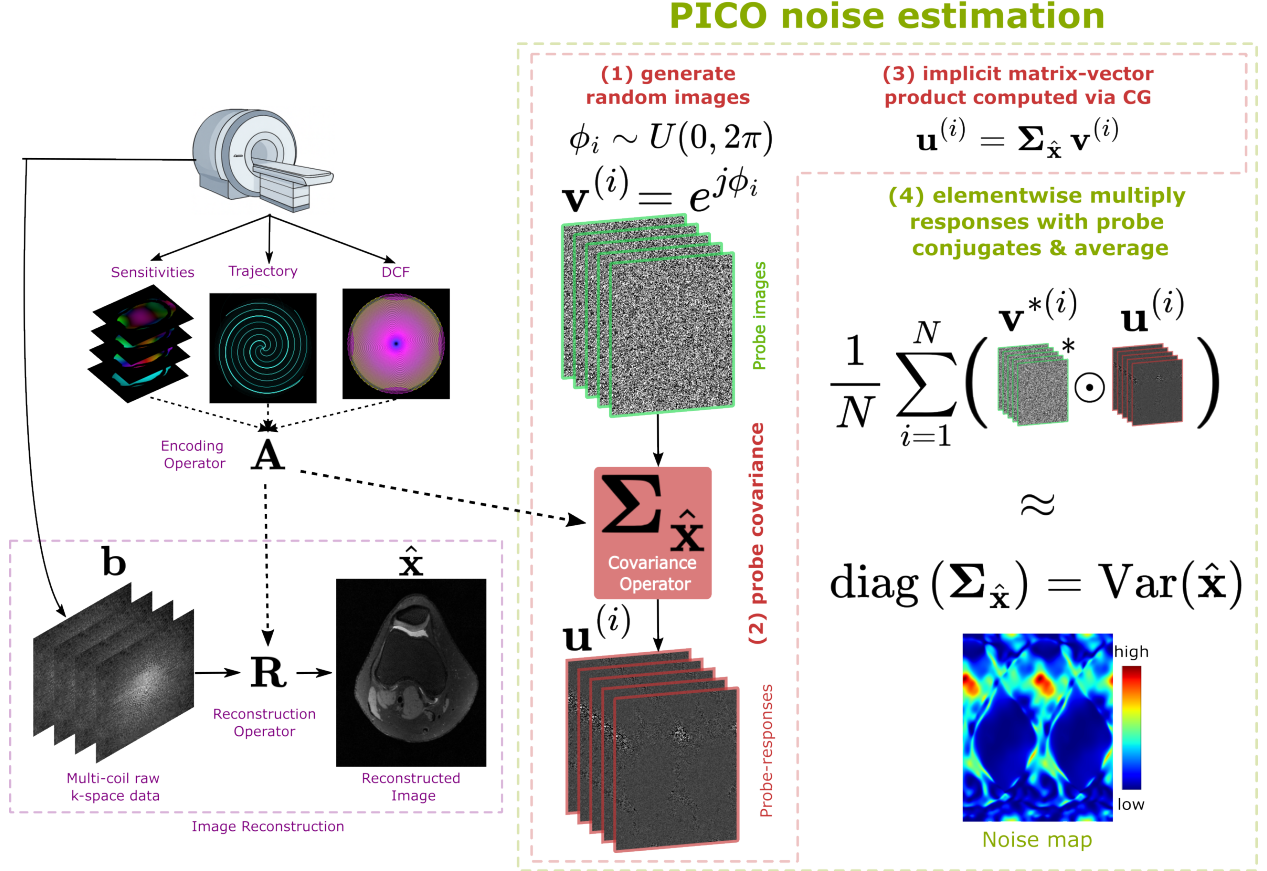


Figure 1: Overview of PICO for fast voxelwise noise characterization. Left: the MRI acquisition is modeled by an encoding operator \mathbf{A} (coil sensitivities, sampling trajectory, density compensation); the reconstruction operator \mathbf{R} maps multi-coil k -space data to the image estimate $\hat{\mathbf{x}}$. Right: PICO estimates the voxelwise noise variance map $\text{diag}(\Sigma_{\hat{\mathbf{x}}})$ in four steps. (1) Generate unit-magnitude random-phase probe images $\mathbf{v}^{(i)}$, $i = 1, \dots, N$. (2) Pass each probe through the implicit covariance operator $\Sigma_{\hat{\mathbf{x}}} = \mathbf{R}\mathbf{R}^H$, without forming the matrix explicitly. (3) Evaluate the covariance–vector product $\mathbf{u}^{(i)} = \Sigma_{\hat{\mathbf{x}}} \mathbf{v}^{(i)}$ via CG on the normal equations, reusing the same \mathbf{A}/\mathbf{A}^H primitives as CG-SENSE reconstruction. (4) Elementwise multiply each response by its probe conjugate and average: $\hat{\sigma}_{\hat{\mathbf{x}}}^2 = \frac{1}{N} \sum_{i=1}^N \mathbf{v}^{(i)*} \odot \mathbf{u}^{(i)}$.

Relative noise amplification (the g -factor) is then defined as:

$$g(i) = \frac{\sigma_{\hat{\mathbf{x}}, \text{acc}, \lambda}(i)}{\sqrt{R} \sigma_{\hat{\mathbf{x}}, \text{ref}}(i)}, \quad (11)$$

where $\sigma_{\hat{\mathbf{x}}, \text{acc}, \lambda}(i)$ is the noise standard deviation of the i -th voxel in the accelerated, regularized reconstruction, and $\sigma_{\hat{\mathbf{x}}, \text{ref}}(i)$ is the corresponding quantity from a fully sampled, reference reconstruction using the same coil configuration.

2.2 Direct Noise Estimation via Probing the Image-Space Covariance (PICO)

To overcome the limitations of PMR, we propose a direct and computationally efficient framework for estimating the voxelwise noise variance map $\sigma_{\hat{\mathbf{x}}}^2 = \text{diag}(\Sigma_{\hat{\mathbf{x}}})$ defined in (10), without performing multiple reconstructions. PICO operates entirely in the image domain and is summarized in Fig. 1. It builds upon stochastic trace and diagonal estimators from numerical linear algebra [35, 36], generalized here to complex Hermitian covariances with $\Sigma_{\hat{\mathbf{x}}} = \mathbf{R}\mathbf{R}^H$.

2.2.1 An unbiased noise variance estimator

The goal is to estimate $\text{diag}(\boldsymbol{\Sigma}_{\hat{\mathbf{x}}})$ without explicitly forming the full covariance matrix. Let $\{\mathbf{v}^{(i)}\}_{i=1}^{N_{\text{probes}}}$ be independent probe images drawn from a distribution with zero mean and identity covariance (examples below). For each probe, define the implicit covariance–vector product

$$\mathbf{u}^{(i)} := \boldsymbol{\Sigma}_{\hat{\mathbf{x}}} \mathbf{v}^{(i)}, \quad (12)$$

which can be evaluated using the same primitives as CG-SENSE (applications of \mathbf{A} , \mathbf{A}^{H} , and regularized normal-equation solves) without forming $\boldsymbol{\Sigma}_{\hat{\mathbf{x}}}$.

The diagonal of $\boldsymbol{\Sigma}_{\hat{\mathbf{x}}}$ is then estimated via elementwise products of probe conjugates and responses:

$$\widehat{\text{diag}}(\boldsymbol{\Sigma}_{\hat{\mathbf{x}}}) = \frac{1}{N_{\text{probes}}} \sum_{i=1}^{N_{\text{probes}}} \mathbf{v}^{(i)*} \odot \mathbf{u}^{(i)}. \quad (13)$$

By identification with (10), we write the *estimated noise variance map* as

$$\hat{\boldsymbol{\sigma}}_{\hat{\mathbf{x}}}^2 := \widehat{\text{diag}}(\boldsymbol{\Sigma}_{\hat{\mathbf{x}}}) = \frac{1}{N_{\text{probes}}} \sum_{i=1}^{N_{\text{probes}}} \mathbf{v}^{(i)*} \odot (\boldsymbol{\Sigma}_{\hat{\mathbf{x}}} \mathbf{v}^{(i)}). \quad (14)$$

2.2.2 Unbiasedness

Assume the probe distribution satisfies

$$\mathbb{E}[\mathbf{v}^{(i)}] = \mathbf{0}, \quad \mathbb{E}[\mathbf{v}^{(i)}(\mathbf{v}^{(i)})^{\text{H}}] = \mathbf{I}. \quad (15)$$

Let $\mathbf{y}^{(i)} = \mathbf{v}^{(i)*} \odot \mathbf{u}^{(i)}$ with $\mathbf{u}^{(i)} = \boldsymbol{\Sigma}_{\hat{\mathbf{x}}} \mathbf{v}^{(i)}$. For the k -th voxel,

$$y_k^{(i)} = v_k^{(i)*} \sum_j (\boldsymbol{\Sigma}_{\hat{\mathbf{x}}})_{kj} v_j^{(i)}$$

$$\mathbb{E}[y_k^{(i)}] = \sum_j (\boldsymbol{\Sigma}_{\hat{\mathbf{x}}})_{kj} \mathbb{E}[v_k^{(i)*} v_j^{(i)}] = (\boldsymbol{\Sigma}_{\hat{\mathbf{x}}})_{kk}. \quad (16)$$

Thus $\mathbb{E}[\mathbf{y}^{(i)}] = \text{diag}(\boldsymbol{\Sigma}_{\hat{\mathbf{x}}})$, and averaging in (14) yields an unbiased estimator of the noise variance map:

$$\mathbb{E}[\hat{\boldsymbol{\sigma}}_{\hat{\mathbf{x}}}^2] = \text{diag}(\boldsymbol{\Sigma}_{\hat{\mathbf{x}}}) = \boldsymbol{\sigma}_{\hat{\mathbf{x}}}^2. \quad (17)$$

The estimator variance decreases as $1/N_{\text{probes}}$. For a detailed analysis of the theoretical properties of the estimator, see Appendix B and C.

2.2.3 Implicit matrix–vector product via CG

The vector $\mathbf{u}^{(i)}$ in (12) is not computed by explicitly forming $\boldsymbol{\Sigma}_{\hat{\mathbf{x}}}$, which would be intractable for realistic image sizes. Instead, it is obtained implicitly using operator access to the reconstruction operator \mathbf{R} and its adjoint \mathbf{R}^{H} , both of which are naturally available within iterative solvers such as CG-SENSE. Since \mathbf{R} itself corresponds to a linear mapping, the product $\mathbf{u}^{(i)} = \boldsymbol{\Sigma}_{\hat{\mathbf{x}}} \mathbf{v}^{(i)} = \mathbf{R}(\mathbf{R}^{\text{H}} \mathbf{v}^{(i)})$ can be efficiently evaluated through existing forward and adjoint operations without ever forming $\boldsymbol{\Sigma}_{\hat{\mathbf{x}}}$ explicitly. In practice, this implicit computation is implemented using the same low-level routines that perform the CG-SENSE reconstruction, requiring only matrix–vector products with \mathbf{A} and \mathbf{A}^{H} and regularized normal-equation solves. A complete algorithmic pseudocode description of PICO is provided in Appendix A.

2.2.4 Choice of probing vectors

Several families of random vectors satisfy the probe conditions in (15). The single-sample variance of the diagonal estimator at each voxel decomposes into two contributions (Appendix B): one that scales with the kurtosis $\kappa = \mathbb{E}[|v_k|^4]$ of the probe distribution and multiplies the squared diagonal entries $|(\boldsymbol{\Sigma}_{\hat{\mathbf{x}}})_{kk}|^2$, and one that depends only on the off-diagonal energy $\sum_{\ell \neq k} |(\boldsymbol{\Sigma}_{\hat{\mathbf{x}}})_{k\ell}|^2$ and is invariant across probe distributions. Minimizing the per-sample variance therefore reduces to minimizing the kurtosis κ subject to the unit-variance constraint $\mathbb{E}[|v_k|^2] = 1$.

A natural baseline is the standard complex Gaussian probe,

$$\mathbf{v}^{(i)} \sim \mathcal{CN}(\mathbf{0}, \mathbf{I}), \quad (18)$$

which satisfies $\kappa = 2$. Prior work on real-valued diagonal estimation showed that Rademacher probes [35, 36],

$$v_k^{(i)} \in \{-1, +1\}, \quad \mathbb{P}(v_k^{(i)} = +1) = \mathbb{P}(v_k^{(i)} = -1) = \frac{1}{2}, \quad (19)$$

attain $\kappa = 1$, halving the diagonal contribution to the per-sample variance relative to Gaussian probes. Since $\kappa = 1$ is the smallest kurtosis achievable by any unit-variance distribution, real Rademacher probes are already kurtosis-optimal for real-valued covariance operators.

For the complex Hermitian covariances $\boldsymbol{\Sigma}_{\hat{\mathbf{x}}}$ that arise in MRI reconstruction, however, real-valued probes are information-limited: a real probe encodes only one real degree of freedom per voxel, leaving the imaginary components of the off-diagonal entries $(\boldsymbol{\Sigma}_{\hat{\mathbf{x}}})_{k\ell}$ invisible to a single sample, so that two independent real probes are required to capture the same information as a single complex probe (Appendix B). We therefore adopt the complex analogue of the Rademacher distribution: unit-magnitude probes with uniformly distributed phase,

$$v_k^{(i)} = e^{j\theta_k^{(i)}}, \quad \theta_k^{(i)} \sim \text{Uniform}[0, 2\pi]. \quad (20)$$

The random-phase distribution satisfies $\mathbb{E}[\mathbf{v}^{(i)}] = \mathbf{0}$ and $\mathbb{E}[\mathbf{v}^{(i)}(\mathbf{v}^{(i)})^H] = \mathbf{I}$ exactly—these conditions are inherent to the construction rather than asymptotic—and attains the same minimum kurtosis $\kappa = 1$ as real Rademacher while encoding two real degrees of freedom per voxel. Random-phase probes therefore strictly minimize the single-sample variance among unit-variance distributions on complex Hermitian operators (Appendix B). We empirically validate this design choice in an ablation study (Sec. 4.2) comparing random-phase, real Rademacher, and complex Gaussian probes at matched probe counts.

2.2.5 Extension to Compressed-Sensing reconstructions

When the reconstruction problem in Eq. (4) is non-smooth (e.g., TV or ℓ_1), the reconstruction map $f : \mathbf{b}_w \mapsto \hat{\mathbf{x}}$ becomes nonlinear [39] and the exact covariance $\text{Cov}[\hat{\mathbf{x}}]$ has no tractable closed form. We employ a local linearization, following the Jacobian-based framework introduced in recent work [32, 33]. Let $\mathbf{k}_0 = \mathbf{A}\mathbf{x}$ denote the noise-free k-space data. If the converged solution $\hat{\mathbf{x}}$ is differentiable with respect to \mathbf{b}_w at \mathbf{k}_0 (which holds almost everywhere for piecewise-linear proximal operators such as soft-thresholding [32, 33]), then

$$f(\mathbf{k}_0 + \mathbf{n}_w) \approx f(\mathbf{k}_0) + \mathbf{J}_f(\mathbf{k}_0) \mathbf{n}_w,$$

and the image-domain noise covariance is approximated as

$$\boldsymbol{\Sigma}_{\hat{\mathbf{x}}} \approx \mathbf{J}_f(\mathbf{k}_0) \mathbf{J}_f(\mathbf{k}_0)^H.$$

This approximation is exact to first order in the noise amplitude and becomes increasingly accurate as the input SNR increases. Consequently, the stochastic diagonal estimator applied to $\mathbf{J}_f \mathbf{J}_f^H$ yields a *locally unbiased* estimate of the noise variance map. Modern automatic differentiation frameworks provide efficient access to Jacobian–vector products, enabling direct evaluation of $\mathbf{u} = \mathbf{J}_f(\mathbf{k}_0) \mathbf{v}$ for random probes \mathbf{v} [32–34].

Therefore, even in the nonlinear CS setting, the stochastic diagonal estimator remains directly applicable: averaging $|\mathbf{u}|^2$ across probes yields unbiased noise variance estimates, and taking the elementwise square root produces voxelwise noise standard deviation maps.

Relationship to the linear case. The Jacobian formulation above subsumes the linear covariance-probing construction of Sec. 2.2.1 as a special case. For a linear reconstruction $\hat{\mathbf{x}} = \mathbf{R}\mathbf{b}_w$, the Jacobian is constant and equal to the reconstruction operator itself, $\mathbf{J}_f(\mathbf{k}_0) = \mathbf{R}$, so that

$$\mathbf{J}_f \mathbf{J}_f^H = \mathbf{R} \mathbf{R}^H = \boldsymbol{\Sigma}_{\hat{\mathbf{x}}}, \quad (21)$$

and the Jacobian-based estimator coincides exactly with direct probing of $\boldsymbol{\Sigma}_{\hat{\mathbf{x}}}$. The proposed framework is therefore a single estimator applied to the same class of Hermitian positive-semidefinite operators in both regimes—exact for linear reconstructions, first-order for nonlinear ones—rather than two distinct methods for two distinct problems. In practice, we use the direct covariance formulation $\boldsymbol{\Sigma}_{\hat{\mathbf{x}}}\mathbf{v} = \mathbf{R}\mathbf{R}^H\mathbf{v}$ for linear reconstructions because it reuses existing CG-SENSE primitives without invoking automatic differentiation, but the two constructions yield mathematically identical results whenever the reconstruction map is linear.

3 Methods

3.1 Datasets

Stanford knee. Eight-channel proton-density-weighted 3D fast-spin-echo knee scans were obtained from `mridata.org` [40]: 14 subjects, acquisition matrix $k_x \times k_y \times k_z = 320 \times 320 \times 256$. All datasets were fully sampled at acquisition. A 1D inverse Fourier transform along readout produced hybrid k-space slices ($x \times k_y \times k_z$). Coil sensitivities were estimated with JSENSE (kernel width 8, 20×20 auto-calibration region) [41]. Quantitative metrics were computed per slice and averaged within each subject; inter-subject statistics are reported over all 14 subjects.

Physical brain phantom. A physical brain phantom was imaged using a gradient-echo spiral acquisition at 1 mm isotropic resolution (22 cm FOV, 60 interleaves) on a GE 3T Ultra High Performance scanner with 13 receive channels. Coil sensitivities were estimated by ESPIRiT from the fully sampled central region [42].

fastMRI knee. Fifteen fully sampled subjects from the fastMRI dataset [43] were used: Cartesian fast spin-echo, 15-channel coronal proton-density fat-suppressed images, matrix $320 \times 320 \times 25$. Coil sensitivities were estimated by ESPIRiT using 24 central auto-calibration lines [42].

3.2 Reconstruction experiments

All experiments assess the accuracy of voxelwise noise variance estimation, with g -factor maps reported as derived ratios where a fully sampled reference is available. For the Cartesian experiment, a closed-form analytical noise reference serves as ground truth; for the non-Cartesian and CS

experiments, where no closed-form reference exists, high-replica PMR maps serve as surrogate references with convergence independently validated (Appendix E). Reconstructed magnitude images are shown alongside noise and g -factor maps for anatomical context. For brevity, N denotes the number of probes (PICO) or replicas (PMR) throughout.

3.2.1 Cartesian CG-SENSE

Experimental setup. The Stanford knee dataset was used to evaluate both methods against an analytical ground truth. Fully sampled multi-coil k-space was retrospectively undersampled along the phase-encoding direction at $R = 2$ (uniform pattern, $R_x = 1$, $R_y = 2$). Undersampled data were reconstructed by CG-SENSE without regularization:

$$\hat{\mathbf{x}} = \arg \min_{\mathbf{x}} \|\mathbf{A}_{\text{acc}}\mathbf{x} - \mathbf{b}_{\text{acc}}\|_2^2,$$

with eigenvalue normalization (15-step power method, $1.01\times$ safety margin) and 25 CG iterations. The closed-form analytical SENSE noise-variance map served as ground-truth reference [11].

Evaluation. Both PICO and PMR were evaluated at probe/replica counts $N \in \{10, 20, 40, 80, 200\}$. Quantitative accuracy was assessed via voxelwise NRMSE at $N = 200$, computed per slice and averaged within each subject. Statistical significance of the NRMSE difference between PICO and PMR was tested using a paired Wilcoxon signed-rank test across the 14 subjects’ per-subject mean NRMSE values (two-sided $p < 0.01$).

3.2.2 Non-Cartesian CG-SENSE

Experimental setup. non-Cartesian multi-coil k-space data from brain phantom was undersampled via retrospective shot subsampling: every R -th interleave was retained, yielding acceleration factors $R \in \{2, 3, 4\}$. Reconstruction solved the Tikhonov-regularized problem [16]:

$$\hat{\mathbf{x}} = \arg \min_{\mathbf{x}} \|\mathbf{A}_{\text{acc}}\mathbf{x} - \mathbf{b}_{\text{acc}}\|_2^2 + \lambda\|\mathbf{x}\|_2^2,$$

with $\lambda = 0.1$, Kaiser–Bessel NUFFT (width 4), Toeplitz normal-operator approximation, eigenvalue normalization (15-step power method, $1.01\times$), and 100 CG iterations (tolerance 10^{-2}).

Estimators and reference. PMR used i.i.d. complex Gaussian noise ($\sigma_k = 10^{-2}$); PICO used random-phase probes. Because no closed-form g -factor exists for non-Cartesian trajectories, a high-fidelity PMR estimate at $N_{\text{ref}} = 30,000$ replicas served as a reference, with convergence independently validated (Appendix E). Benchmarking against PMR’s own converged output, if anything, favors PMR: any residual PMR-specific bias is absorbed into the reference rather than penalized.

Evaluation. Both methods were evaluated from $N = 10$ to $N = 10,000$ in steps of 10. NRMSE was computed against the PMR reference at each N to generate accuracy–runtime trade-off curves. We report the operating point where each method first reached 1% NRMSE. An ablation study compared convergence of three probe distributions (random phase, real Rademacher, standard complex Gaussian) over the same N range.

3.2.3 Compressed-Sensing reconstruction

Experimental setup. Ten subjects’ images from the fastMRI knee dataset were retrospectively undersampled using a Poisson-disc pattern ($R = 2$, 24×24 calibration region). Reconstruction used FISTA [44] with total-variation (TV) regularization [45]:

$$\hat{\mathbf{x}} = \arg \min_{\mathbf{x}} \frac{1}{2} \|\mathbf{A}\mathbf{x} - \mathbf{b}\|_2^2 + \lambda_{\text{TV}} \|\nabla \mathbf{x}\|_1,$$

with $\lambda_{\text{TV}} = 10^{-2}$ and 100 FISTA iterations.

Variance estimation. PICO was applied to the Jacobian of the reconstruction map at the converged solution, evaluating $\mathbf{u} = \mathbf{J}_f(\mathbf{k}_0)\mathbf{v}$ via automatic differentiation [32]. PMR used $\sigma_k = 10^{-7}$.

Evaluation. Because no closed-form noise reference exists for nonlinear reconstructions, convergence was analyzed using method-specific gold-standard references: separate high-sample-count runs at $N = 50,000$ for PICO and for PMR, each used to benchmark its own lower- N estimates (Appendix E). NRMSE was computed on estimated noise standard deviation maps at each intermediate N ; runtime efficiency was quantified by comparing the time for each method to reach converged accuracy. Statistical significance of the NRMSE difference between PICO and PMR was tested using a paired Wilcoxon signed-rank test across the 10 subjects’ per-subject mean NRMSE values.

Robustness to input noise level. To assess validity of the local linearization, the input noise standard deviation was swept over scale factors $\{1, 5, 10, 50, 100, 200\} \times \sigma_0$ ($\sigma_0 = 10^{-7}$), spanning SNR from approximately 45 to -1 dB. For each level, variance maps were computed by both methods at $N = 3000$. Normalized output maps ($\sigma_{\hat{\mathbf{x}}}/\sigma_k$) were compared to test whether PICO remains concordant with PMR across a broad SNR range.

3.3 Implementation details

Software and operators. All methods were implemented in Python/PyTorch with complex64 arithmetic [46]. Non-Cartesian encoding and reconstruction used SigPy [47] (Kaiser-Bessel width 4) with Toeplitz embedding for the normal operator [24]. Cartesian operators used the same NUFFT framework with grid-aligned trajectories.

Solvers. Linear reconstructions used CG on the normal equations; nonlinear CS used FISTA with standard momentum [44]. Spectral normalization (λ_{max} via 15-step power method, $1.01 \times$ margin) was applied to all forward operators.

Hardware and code availability. All experiments ran on an NVIDIA RTX 8000 GPU. Reported timings are wall-clock measurements averaged over multiple runs. Code is available at https://github.com/onat-dalmaz/fast_mri_gfactor.

4 Results

4.1 Cartesian CG-SENSE

Qualitative results. Figure 2 compares PICO with PMR against the closed-form SENSE g -factor on the Cartesian knee dataset ($R = 2$). PICO recovers the global g -factor distribution with as few

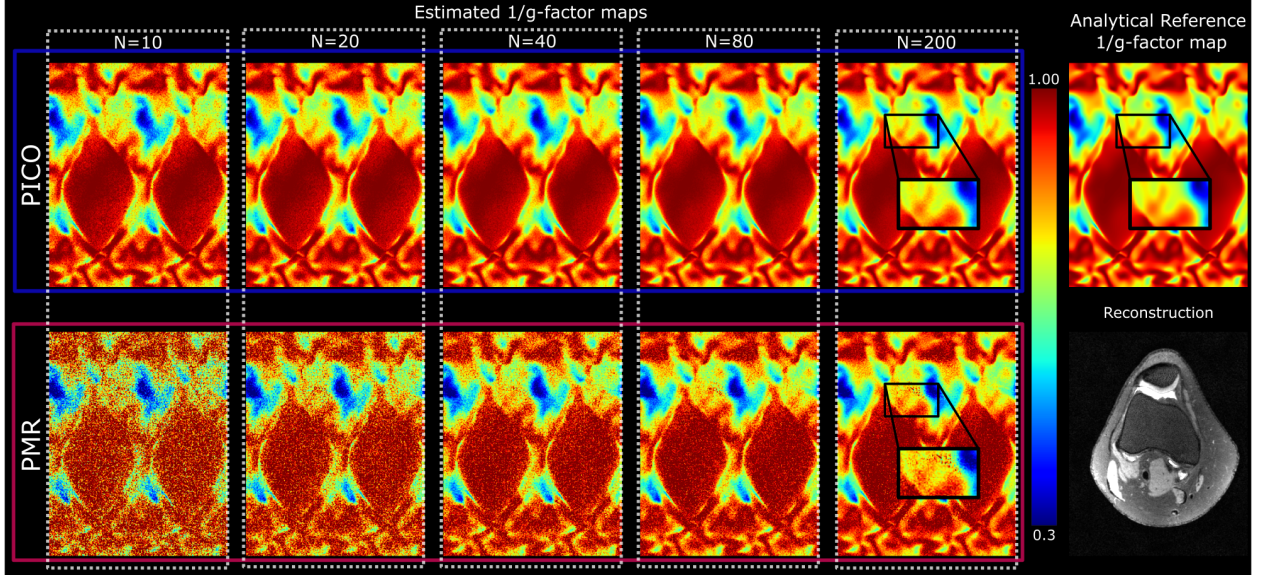


Figure 2: Reciprocal g -factor maps ($1/g$) for Cartesian CG-SENSE at $R = 2$, shown for increasing probe/replica counts ($N = 10, 20, 40, 80, 200$). Top: PICO; bottom: PMR. Right column: analytical SENSE reference (top) and reconstructed magnitude image (bottom). All panels share a fixed color scale set by the analytical reference. PICO recovers the spatial structure of the g -factor by $N = 10$ and is visually converged by $N = 40$ – 80 , whereas PMR retains substantial granular noise through $N = 80$.

as $N = 10$ probes and is visually indistinguishable from the analytical reference by $N = 40$ – 80 ; residual error at low N manifests as low-frequency bias rather than pixel-wise grain. In contrast, PMR exhibits spatially uncorrelated noise that obscures fine structure even at $N = 80$ and only approaches PICO’s smoothness at considerably higher replica counts.

Quantitative results. At $N = 200$, PICO achieved a mean NRMSE of $1.61 \pm 0.19\%$ compared with $8.05 \pm 1.90\%$ for PMR (Wilcoxon $p < 0.01$). Runtime per slice was comparable (13.4 s vs. 16.0 s), with the modest advantage arising because each implicit covariance–vector product converges faster than a full CG-SENSE reconstruction.

4.2 Non-Cartesian CG-SENSE

Qualitative results. Figure 3 shows the convergence of g -factor estimates for the spiral phantom at $R = 2$. The relatively poor conditioning of the non-Cartesian operator requires higher sample counts than the Cartesian case for both methods. PICO resolves the spatial g -factor structure by $N = 1000$; PMR remains dominated by granular noise at the same count and retains visible stochastic texture even at $N = 5000$. Sub-unity g -factors ($g < 1$) appear in some voxels; this is an expected consequence of Tikhonov regularization, which can reduce noise variance below the fully sampled reference (Appendix D).

Quantitative accuracy and runtime. Figure 4 plots NRMSE against wall-clock time on logarithmic axes for all three acceleration factors. At $R = 2$ (Fig. 4a), PICO reached 1% NRMSE in 64.0 s ($N = 800$), compared with 462.6 s ($N = 7950$) for PMR—an approximately $7.2\times$ speedup. At $R = 3$ (Fig. 4b), PICO required $N = 900$ probes (70.6 s) versus $N = 8600$ replicas (501.0 s) for PMR ($\approx 7.1\times$). At $R = 4$ (Fig. 4c), the corresponding figures were $N = 1150$ probes (91.0 s) versus

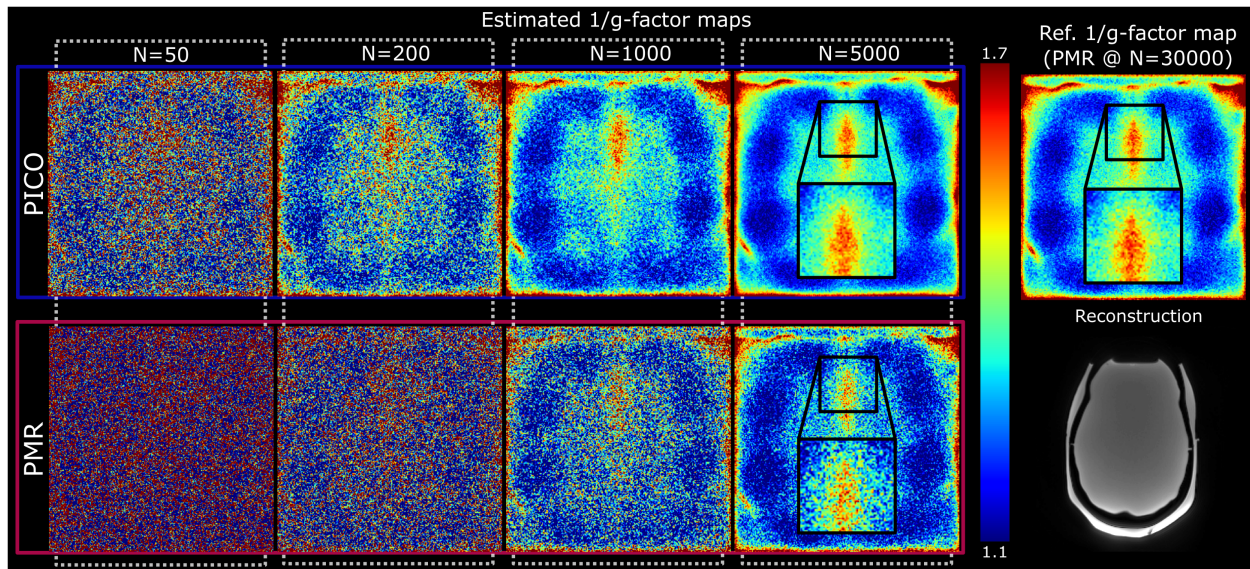


Figure 3: Voxelwise g -factor maps for non-Cartesian CG-SENSE ($R = 2$, spiral trajectory). Columns show increasing sample counts ($N \in \{50, 200, 1000, 5000\}$); right column: PMR reference at $N = 30,000$ and magnitude image. Top: PICO; bottom: PMR. PICO resolves the g -factor structure by $N = 1000$, whereas PMR retains visible Monte Carlo artifacts even at $N = 5000$.

$N = 9400$ replicas (538.6 s; $\approx 5.9\times$). Across all acceleration factors, going from $R = 2$ to $R = 4$ required only 350 additional probes for PICO versus 1450 additional replicas for PMR, consistent with the theoretical prediction that PMR’s estimator variance scales quadratically with local noise variance (Appendix C).

Probe distribution ablation. Figure 5 compares the three probe distributions on the spiral dataset. At every N , random phase probes yielded the lowest NRMSE, followed by real-valued Rademacher, then complex Gaussian—consistent with the kurtosis-based variance analysis in Appendix B.

4.3 Compressed-Sensing reconstruction

Accuracy and efficiency. Figure 6 compares noise standard deviation maps from PICO and PMR. The maps are visually indistinguishable, both capturing the data-dependent noise texture characteristic of TV regularization (suppression in uniform regions, preservation near edges). Across the dataset, PICO required 52.3 ± 7.7 s compared with 95.5 ± 14.0 s for PMR, a statistically significant $\approx 1.8\times$ speedup (Wilcoxon $p < 0.05$).

Robustness to input noise level. Figure 7 shows normalized output noise maps across a range of input noise amplitudes ($\text{SNR} \approx 45$ to -1 dB). Under a valid local linear model, the normalized map $\sigma_{\hat{x}}/\sigma_k$ is expected to remain stationary. At moderate-to-high SNR (≥ 16 dB), PICO and PMR exhibit negligible differences, even in $\times 10$ amplified views. At extreme noise levels ($\text{SNR} \leq 4$ dB)—well below the SNR range encountered in standard acquisitions [48, 49]—the local linear approximation shows visible residual structure, as the active set of the TV proximal operator fluctuates substantially across noise realizations. Even in these stress-test conditions, however, the estimator correctly identifies the dominant heteroscedastic noise amplification patterns, and

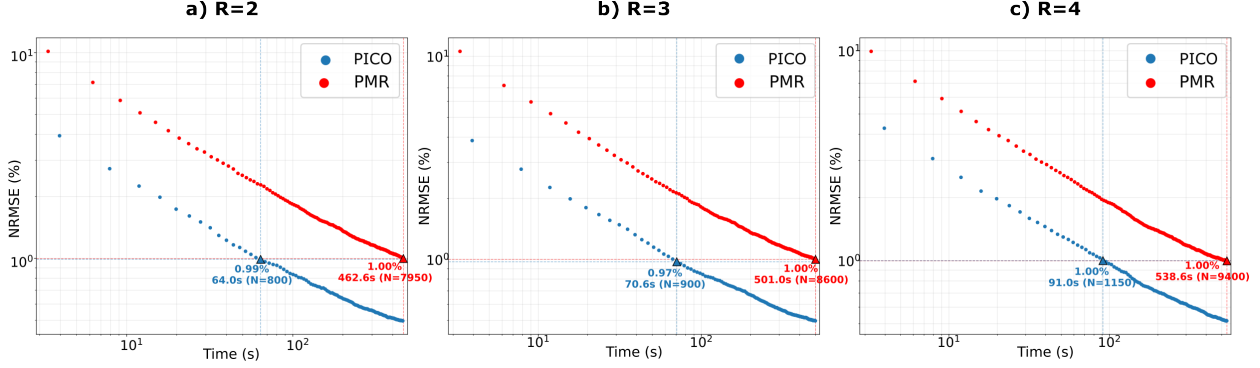


Figure 4: NRMSE vs. runtime for non-Cartesian CG-SENSE (log–log scale). **(a)** $R = 2$: PICO reaches 1% NRMSE in 64.0 s ($N = 800$); PMR requires 462.6 s ($N = 7950$). **(b)** $R = 3$: proposed 70.6 s ($N = 900$) vs. PMR 501.0 s ($N = 8600$). **(c)** $R = 4$: proposed 91.0 s ($N = 1150$) vs. PMR 538.6 s ($N = 9400$). Dashed line: 1% NRMSE threshold; triangles: first crossing for each method.

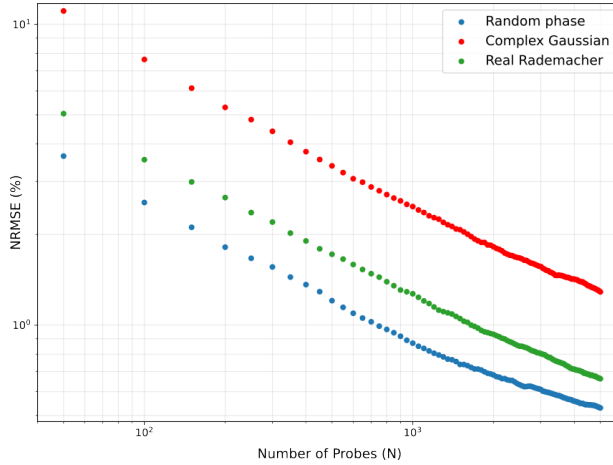


Figure 5: NRMSE vs. probe count N for three probe families on non-Cartesian CG-SENSE (log–log scale). Random phase (blue) achieves the lowest error at every N , followed by real Rademacher (green) and complex Gaussian (red), confirming the theoretical optimality of unit-magnitude random-phase probes. All three distributions exhibit approximately parallel power-law decay, with the vertical offset governed by the probe kurtosis (Appendix B).

departures from linearity manifest as second-order effects.

5 Discussion

PICO versus PMR: from k -space perturbation to image-space probing. Image-Space Covariance Probing (PICO) differs from PMR in where randomness enters the pipeline, and this choice drives both the computational and statistical advantages observed in our experiments. PMR perturbs k -space and re-runs a full reconstruction per replica, treating the reconstruction as an opaque simulator of noise propagation [27, 32, 33]. PICO shifts the randomness to image space and works with the noise-propagation operator directly: in the linear case, estimating $\text{diag}(\Sigma_{\tilde{\mathbf{x}}})$ is reduced to passing unit-magnitude random-phase probe images through $\Sigma_{\tilde{\mathbf{x}}}$; in the nonlinear case, we linearize the reconstruction map at the converged solution and use Jacobian–vector products. In both regimes, each probe evaluation reuses the same fast primitives already built for reconstruction

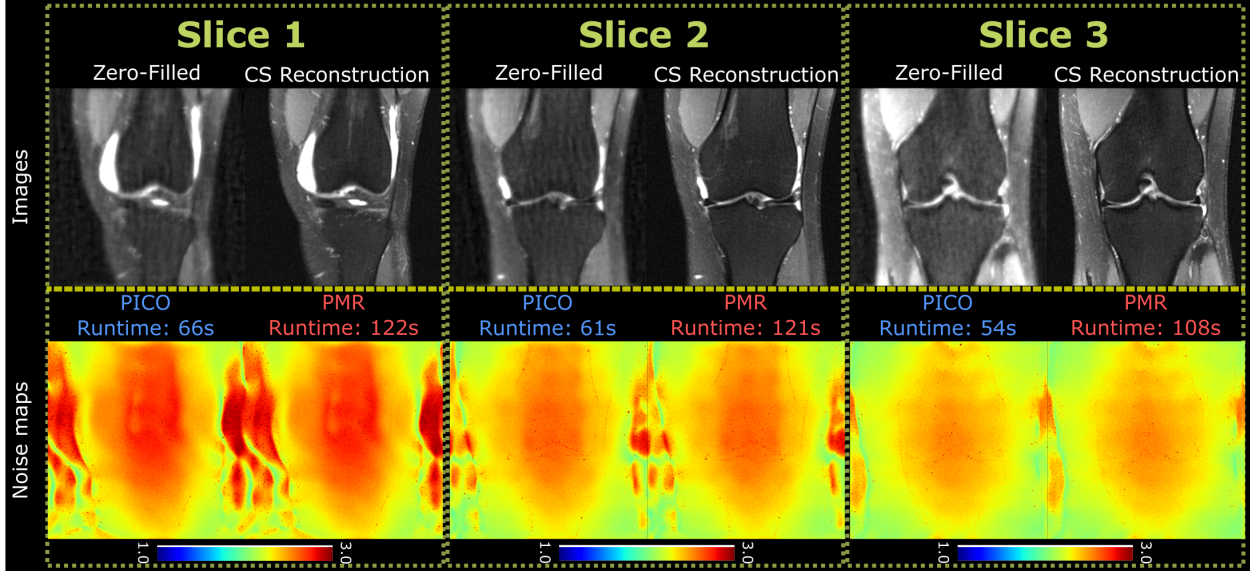


Figure 6: Noise standard deviation maps for TV-regularized CS reconstruction ($R = 2$). Top: zero-filled and CS magnitude images. Bottom: noise maps from PICO (left) and PMR (right), with slice-specific runtimes. The two methods produce visually identical maps; PICO converges faster (e.g., 66 s vs. 122 s for Slice 1).

(\mathbf{A} , \mathbf{A}^H , Toeplitz normal operators, inner CG steps), avoiding repeated end-to-end solves. A second advantage is estimator variance: diagonal estimators admit low-variance probe distributions for Hermitian positive-semidefinite operators [35, 50], and unit-magnitude random-phase probes used by PICO achieve the minimum possible kurtosis ($\kappa = 1$), halving the per-sample variance relative to Gaussian probes (Appendix B). Empirically, this yields lower estimator variance at fixed N and shorter time-to-target accuracy than PMR across all experiments.

Convergence in non-Cartesian settings. Both methods converge more slowly in non-Cartesian reconstructions than in the Cartesian case, reflecting the more globally coupled encoding: NUFFT interpolation and trajectory-dependent point-spread sidelobes spread each noise perturbation over larger spatial neighborhoods, requiring more samples to average out the resulting leakage. For PICO, this manifests as increased off-diagonal energy in $\Sigma_{\hat{\mathbf{x}}}$, which governs the estimator variance (Appendix C). PMR suffers an additional penalty: because it estimates variance from squared magnitudes of complex-Gaussian outputs, individual replicas in high- g -factor regions can produce disproportionately large fluctuations. These heavy-tailed outliers move the sample variance estimate, requiring substantially more replicas before the map stabilizes, yielding a substantial efficiency advantage across all tested acceleration factors (Fig. 4).

Practical implications. The speed of PICO enables noise-mapping workflows that are impractical with PMR. In protocol design, fast noise maps enable direct comparison of candidate acquisition configurations—e.g., evaluating how acceleration factor, phase-encoding direction, or coil layout affects local SNR in a target anatomy—without acquiring and reconstructing full datasets for each option [13, 51]. This is particularly valuable for non-Cartesian trajectories, where no closed-form g -factor formulas exist and protocol tuning has relied on intuition or time-consuming PMR simulations. At scan time, noise maps can identify degraded coil elements or suboptimal patient positioning before the patient leaves the scanner [5]. For regularized reconstructions, voxelwise noise maps offer a principled alternative to global heuristics for selecting λ : one can monitor how the spatial noise

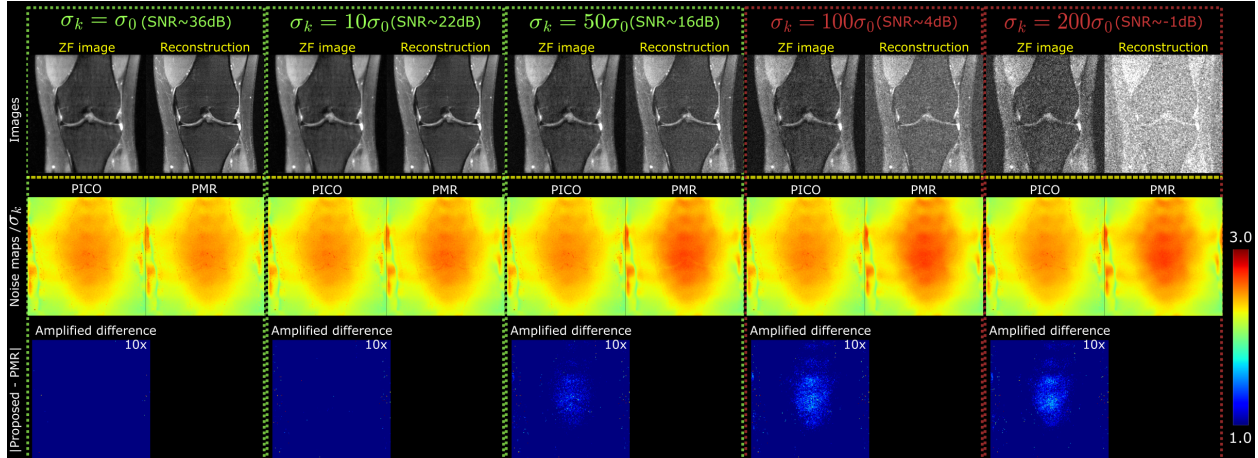


Figure 7: Robustness to input noise level in nonlinear CS reconstruction ($N = 3000$). Columns sweep the noise standard deviation from σ_0 to $200\sigma_0$ ($\text{SNR} \approx 45$ to -1 dB). Top: magnitude images. Middle: normalized noise maps ($\sigma_{\text{out}}/\sigma_k$) from PICO and PMR. Bottom: absolute difference and $\times 10$ amplified view. At moderate-to-high SNR (≥ 16 dB), the two methods agree closely. At extreme noise levels (≤ 4 dB), residual discrepancies reflect higher-order nonlinear effects beyond the first-order Jacobian model.

distribution evolves as λ varies and select the operating point that achieves a desired local SNR floor [52, 53]. In multi-site and longitudinal studies, standardized g -factor reporting would strengthen reproducibility of quantitative biomarkers [54, 55]; PICO could serve as a fast back-end within automated SNR evaluation platforms [56], which currently rely on PMR-based methods and would benefit from the reduced computation time. More broadly, PICO could become a computational tool for the wide range of SNR characterization studies that have so far relied on simple Cartesian acquisitions with closed-form noise models—for example, the relative-SNR comparisons between supine and prone breast coil configurations [57], which currently depend on Cartesian body-coil normalization and would benefit from voxelwise noise maps that generalize to arbitrary trajectories and reconstruction methods.

Because PICO averages independent probe contributions, the empirical variance across probes provides a natural online convergence diagnostic: one can monitor the per-voxel standard error of the running mean and stop adding probes when it falls below a user-defined threshold. In the present work, we used fixed N for clean benchmarking against PMR, but an adaptive stopping rule based on the estimator’s own variance would reduce computational cost in practice and could be implemented without additional reconstruction calls. The theoretical variance decomposition (Appendix B, Eq. (A1)) quantifies the expected convergence rate as a function of probe count and covariance structure, providing a principled basis for such adaptive strategies.

Additional computational savings would be possible by estimating variance on a reduced-resolution grid—noise maps are governed primarily by coil geometry and vary more smoothly than anatomical content—and interpolating back to native resolution, a strategy compatible with both the proposed estimator and PMR but most effective when combined with the lower per-probe cost of PICO.

Extensions beyond voxelwise variance. This work focuses on the diagonal of the image-domain covariance, consistent with the standard definition of the g -factor and most prior noise-analysis literature [11, 13, 27, 29, 32]. However, the off-diagonal entries—capturing spatial cross-correlations between voxels—encode complementary information relevant to applications such as functional

connectivity estimation in fMRI, where structured covariance is the central object of interest [58, 59]. Extending the framework to approximate selected off-diagonal terms or low-rank covariance structure could link acquisition and reconstruction choices to downstream connectivity metrics. A related direction is propagating reconstruction-induced noise through parameter-estimation pipelines (e.g., T_1/T_2 mapping, diffusion) to obtain spatiotemporal uncertainty maps rather than a single static g -factor slice; recent work on dictionary-based quantitative MRI has demonstrated the value of explicitly quantifying matching uncertainty [60].

Leveraging noise maps in downstream imaging tasks. Beyond reconstruction diagnostics, voxelwise noise-variance maps can be consumed directly by downstream processing. Classical adaptive filters (e.g., BM3D) use local variance to tune denoising thresholds [61, 62], and spatially varying noise estimates have improved content in low-dose CT and ultrasound [63, 64]. In deep-learning settings, feeding noise or uncertainty maps as additional input channels or using them for loss reweighting has been reported to reduce false positives and improve calibration [34, 65, 66]. Recent work has demonstrated that providing g -factor maps directly as network inputs—together with SNR-unit-normalized images—yields architecture-agnostic denoising improvements and strong generalization across field strengths, contrasts, and anatomies [67, 68]. Those methods rely on closed-form GRAPPA-based g -factor computation, which is confined to Cartesian acquisitions, and revert to PMR for measuring output noise when evaluating the trained denoisers. PICO extends this capability in two ways: first, by making voxelwise noise maps available for non-Cartesian and nonlinear reconstruction pipelines where analytical g -factor formulas are unavailable, potentially enabling SNR-aware denoising for a broader class of acquisitions; and second, by replacing the PMR-based output-noise measurement step with a faster and lower-variance alternative. Systematically coupling fast noise estimation with variance-aware filters and networks, and quantifying the benefit over simpler heuristic noise models under aggressive acceleration, is an important direction for future work.

Limitations. Although PICO achieves improved g -factor and noise estimation relative to PMR under matched computation time, this work does not directly assess how the improvements translate to observer perception or task-based diagnostic performance. Classical parallel-imaging studies have evaluated g -factor maps as physics-based summary metrics rather than tools inspected alongside images [13, 51, 69], yet broader literature on task-based image quality shows that objective noise measures can diverge from radiologist preferences [70–73]. Prospective reader studies that define application-specific operating points—how much estimator accuracy is needed before perceived noise texture and lesion conspicuity stop improving—would help align noise estimation research with downstream decision-making. A second limitation is the Jacobian-based approximation for nonlinear reconstructions, which is valid to first order in the noise amplitude. Our robustness experiments (Fig. 7) confirm close agreement with PMR at moderate-to-high SNR, but at extreme noise levels the local linear model shows visible residual error. Extending the framework to capture higher-order nonlinear effects, or to provide formal uncertainty bounds on the linearization error itself, remains an open problem. A third direction is operator-aware probe design: random-phase probes are optimal among distributions (Appendix B), but optimized probes that exploit the covariance’s structure [36] could further reduce estimator variance.

6 Conclusion

We have presented a stochastic diagonal estimation framework for fast, voxelwise noise variance and g -factor mapping in MRI reconstructions. For linear reconstructions such as CG-SENSE—including the unaccelerated case—the method recovers the exact diagonal of the image-domain noise covariance without any model approximation; for nonlinear reconstructions (e.g., compressed sensing with TV regularization), it extends naturally through Jacobian–vector products. In both settings, unit-magnitude random-phase probes provably minimize the per-sample estimator variance.

Across Cartesian, non-Cartesian, and compressed-sensing experiments, PICO matched or exceeded the accuracy of high-replica PMR references while requiring a fraction of the computation time. These results demonstrate that rigorous noise characterization need not be a computational bottleneck: the same operator primitives used for image reconstruction can be reused to produce voxelwise SNR maps as a routine by-product of the reconstruction pipeline. We anticipate that embedding fast noise estimation into standard MRI workflows will support protocol optimization, quality assurance, and downstream uncertainty-aware analysis across a broad range of reconstruction methods.

Data Availability Statement

All image data, source code for reconstruction experiments, and noise estimation toolbox are publicly available at https://github.com/onat-dalmaz/pico_noise_estimation_toolbox.

References

- [1] Albert Macovski. Noise in mri. *Magnetic Resonance in Medicine*, 36(3):494–497, 1996. doi: <https://doi.org/10.1002/mrm.1910360327>. URL <https://onlinelibrary.wiley.com/doi/abs/10.1002/mrm.1910360327>.
- [2] P. B. Roemer, W. A. Edelstein, C. E. Hayes, S. P. Souza, and O. M. Mueller. The nmr phased array. *Magnetic Resonance in Medicine*, 16(2):192–225, 1990. doi: <https://doi.org/10.1002/mrm.1910160203>. URL <https://onlinelibrary.wiley.com/doi/abs/10.1002/mrm.1910160203>.
- [3] Olaf Dietrich, José G. Raya, Scott B. Reeder, Michael Ingrisch, Maximilian F. Reiser, and Stefan O. Schoenberg. Influence of multichannel combination, parallel imaging and other reconstruction techniques on mri noise characteristics. *Magnetic Resonance Imaging*, 26(6):754–762, 2008. ISSN 0730-725X. doi: <https://doi.org/10.1016/j.mri.2008.02.001>. URL <https://www.sciencedirect.com/science/article/pii/S0730725X08000337>.
- [4] Olaf Dietrich, José G. Raya, Scott B. Reeder, Maximilian F. Reiser, and Stefan O. Schoenberg. Measurement of signal-to-noise ratios in mr images: Influence of multichannel coils, parallel imaging, and reconstruction filters. *Journal of Magnetic Resonance Imaging*, 26:375–385, 8 2007. ISSN 10531807. doi: 10.1002/jmri.20969.
- [5] Peter Kellman and Elliot R. McVeigh. Image reconstruction in snr units: A general method for snr measurement. *Magnetic Resonance in Medicine*, 54:1439–1447, 2005. ISSN 07403194. doi: 10.1002/mrm.20713.
- [6] James D. Rubenstein, John M. Brown, John C. Kohn, and Steven P. Arnoczky. Cartilage invasion by fat: A possible mechanism of steroid-induced osteonecrosis? *American Journal*

- of *Roentgenology*, 169(6):1439–1441, 1997. doi: 10.2214/ajr.169.6.9393162. URL <https://www.ajronline.org/doi/10.2214/ajr.169.6.9393162>.
- [7] R. A. Lerski and J. D. de Certaines. Performance assessment and quality control in mri by eurospin test objects and protocols. *Magnetic Resonance Imaging*, 11(6):817–833, 1993. doi: 10.1016/0730-725X(93)90199-N. URL <https://pubmed.ncbi.nlm.nih.gov/8371637/>.
- [8] Shingo Kiryu, Hiroyuki Abe, Yusuke Hara, Takayuki Shimizu, Yoshitaka Narita, and Hiroshi Fujita. Deep learning: A primer for radiologists. *RadioGraphics*, 43(1):e1–e15, 2023. doi: 10.1148/rg.211719. URL <https://pubs.rsna.org/doi/10.1148/rg.211719>.
- [9] Florian Knoll, Jure Zbontar, Anuroop Sriram, Matthew J. Muckley, Mary Bruno, Aarn Defazio, Marc Parente, Krzysztof J. Geras, Je Katsnelson, Hersch Chandarana, Zizhao Zhang, Michal Drdzal, Adriana Rmer, Michael Rabbat, Pascal Vincent, James Pinkerton, Duo Wang, Nafissa Yakubova, Erich Owens, C. Lawrence Zitnick, Michael P. Recht, Daniel K. Sodickson, and Yvonne W. Lui. Fastmri: A publicly available raw k-space and dicom dataset of knee images for accelerated mr image reconstruction using machine learning. *Radiology: Artificial Intelligence*, 2, 1 2020. ISSN 26386100. doi: 10.1148/ryai.2020190007.
- [10] Alexander R. Toews, Philip K. Lee, Krishna S. Nayak, and Brian A. Hargreaves. Comprehensive assessment of nonuniform image quality: Application to imaging near metal. *Magnetic Resonance in Medicine*, 92(6):2358–2372, 2024. doi: <https://doi.org/10.1002/mrm.30222>. URL <https://onlinelibrary.wiley.com/doi/abs/10.1002/mrm.30222>.
- [11] Klaas P. Pruessmann, Markus Weiger, Markus B. Scheidegger, and Peter Boesiger. Sense: Sensitivity encoding for fast mri. *Magnetic Resonance in Medicine*, 42:952–962, 1999. ISSN 07403194. doi: 10.1002/(SICI)1522-2594(199911)42:5<952::AID-MRM16>3.0.CO;2-S.
- [12] Daniel K. Sodickson, Mark A. Griswold, Peter M. Jakob, Robert R. Edelman, and Warren J. Manning. Signal-to-noise ratio and signal-to-noise efficiency in smash imaging. *Magnetic Resonance in Medicine*, 41:1009–1022, 1999. ISSN 07403194. doi: 10.1002/(SICI)1522-2594(199905)41:5<1009::AID-MRM21>3.0.CO;2-4.
- [13] Felix A. Breuer, Stephan A.R. Kannengiesser, Martin Blaimer, Nicole Seiberlich, Peter M. Jakob, and Mark A. Griswold. General formulation for quantitative g-factor calculation in GRAPPA reconstructions. *Magnetic Resonance in Medicine*, 62(3):739–746, 2009. doi: 10.1002/mrm.22066.
- [14] Yasuyuki Kurihara, Yoshiko K. Yakushiji, Ichiro Tani, Yasuo Nakajima, and Marc Van Cauteren. Coil sensitivity encoding in mr imaging. *American Journal of Roentgenology*, 178(5):1087–1091, 2002. doi: 10.2214/ajr.178.5.1781087. URL <https://doi.org/10.2214/ajr.178.5.1781087>. PMID: 11959706.
- [15] Frank L. Goerner and Geoffrey D. Clarke. Measuring signal-to-noise ratio in partially parallel imaging mri. *Medical Physics*, 38:5049–5057, 2011. ISSN 00942405. doi: 10.1118/1.3618730.
- [16] Klaas P. Pruessmann, Markus Weiger, Peter Börnert, and Peter Boesiger. Advances in sensitivity encoding with arbitrary k-space trajectories. *Magnetic Resonance in Medicine*, 46:638–651, 2001. ISSN 07403194. doi: 10.1002/mrm.1241.
- [17] Roland Bammer, Murat Aksoy, and Chunlei Liu. Augmented generalized sense reconstruction to correct for rigid body motion. *Magnetic Resonance in Medicine*, 57(1):90–102, 2007. doi:

- <https://doi.org/10.1002/mrm.21106>. URL <https://onlinelibrary.wiley.com/doi/abs/10.1002/mrm.21106>.
- [18] Oliver Maier, Steven Hubert Baete, Alexander Fyrdahl, Kerstin Hammernik, Seb Harrevelt, Lars Kasper, Agah Karakuzu, Michael Loecher, Franz Patzig, Ye Tian, Ke Wang, Daniel Gallichan, Martin Uecker, and Florian Knoll. Cg-sense revisited: Results from the first ismrm reproducibility challenge. *Magnetic Resonance in Medicine*, 85(4):1821–1839, 2021. doi: <https://doi.org/10.1002/mrm.28569>. URL <https://onlinelibrary.wiley.com/doi/abs/10.1002/mrm.28569>.
- [19] Oren N Jaspan, Roman Fleysheer, and Michael L Lipton. Compressed sensing mri: a review of the clinical literature. *British Journal of Radiology*, 88(1056):20150487, 10 2015. ISSN 0007-1285. doi: 10.1259/bjr.20150487. URL <https://doi.org/10.1259/bjr.20150487>.
- [20] Shreyas S. Vasanawala, Marcus T. Alley, Brian A. Hargreaves, Richard A. Barth, John M. Pauly, and Michael Lustig. Improved pediatric mr imaging with compressed sensing. *Radiology*, 256(2):607–616, 2010. doi: 10.1148/radiol.10091218. URL <https://doi.org/10.1148/radiol.10091218>. PMID: 20529991.
- [21] Kerstin Hammernik, Thomas Küstner, Burhaneddin Yaman, Zhengnan Huang, Daniel Rueckert, Florian Knoll, and Mehmet Akçakaya. Physics-driven deep learning for computational magnetic resonance imaging: Combining physics and machine learning for improved medical imaging. *IEEE Signal Processing Magazine*, 40(1):98–114, 2023. doi: 10.1109/MSP.2022.3215288.
- [22] Reinhard Heckel, Mathews Jacob, Akshay Chaudhari, Or Perlman, and Efrat Shimron. Deep learning for accelerated and robust MRI reconstruction. *Magnetic Resonance Materials in Physics, Biology and Medicine*, 37(3):335–368, July 2024. doi: 10.1007/s10334-024-01173-8. URL <https://doi.org/10.1007/s10334-024-01173-8>.
- [23] Klaas P Pruessmann, Markus Weiger, Markus B Scheidegger, and Peter Boesiger. Sense: Sensitivity encoding for fast mri. *Magnetic Resonance in Medicine*, 42:952–962, 1999. ISSN 07403194. doi: 10.1002/(SICI)1522-2594(199911)42:5<952::AID-MRM16>3.0.CO;2-S.
- [24] J.A. Fessler, Sangwoo Lee, V.T. Olafsson, H.R. Shi, and D.C. Noll. Toeplitz-based iterative image reconstruction for mri with correction for magnetic field inhomogeneity. *IEEE Transactions on Signal Processing*, 53(9):3393–3402, 2005. doi: 10.1109/TSP.2005.853152.
- [25] Per Thunberg and Per Zetterberg. Noise distribution in sense- and grappa-reconstructed images: a computer simulation study. *Magnetic Resonance Imaging*, 25:1089–1094, 9 2007. ISSN 0730725X. doi: 10.1016/j.mri.2006.11.003.
- [26] Eros Montin and Riccardo Lattanzi. Seeking a widely adoptable practical standard to estimate signal-to-noise ratio in magnetic resonance imaging for multiple-coil reconstructions. *J. Magn. Reson. Imaging*, 54(6):1952–1964, 2021. doi: 10.1002/jmri.27816.
- [27] Philip M. Robson, Aaron K. Grant, Ananth J. Madhuranthakam, Riccardo Lattanzi, Daniel K. Sodickson, and Charles A. McKenzie. Comprehensive quantification of signal-to-noise ratio and g-factor for image-based and k-space-based parallel imaging reconstructions. *Magnetic Resonance in Medicine*, 60(4):895–907, 2008. doi: <https://doi.org/10.1002/mrm.21728>. URL <https://onlinelibrary.wiley.com/doi/abs/10.1002/mrm.21728>.

- [28] Onat Dalmaz, Arjun Divyang Desai, Akshay Chaudhari, and Brian Hargreaves. Noise-induced variability quantification in deep learning-based mri reconstructions. In *2024 ISMRM and ISMRT Annual Meeting and Exhibition*, Singapore, Singapore, May 2024. ISMRM. URL <http://echo.ismrm.org/abstracts/view/4d1e145f-9b3a-4949-9121-1f5d15f99c48>. Program Number: 2785.
- [29] Mehmet Akcakaya, Tamer A. Basha, Warren J. Manning, and Reza Nezafat. Efficient calculation of g-factors for cg-sense in high dimensions: noise amplification in random undersampling. *Journal of Cardiovascular Magnetic Resonance*, 16, 1 2014. ISSN 1532429X. doi: 10.1186/1532-429X-16-S1-W28.
- [30] Pierre Daudé, Susan Schnell, Caroline Wu, Aurelien B. Kerr, Petter Dyverfeldt, Charles J. François, Michael Markl, Brian A. Hargreaves, and Krishna S. Nayak. Inline automatic quality control of 2D phase-contrast flow MR imaging for subject-specific scan time adaptation. *Magn. Reson. Med.*, 92(2):908–922, 2024. doi: 10.1002/mrm.30083.
- [31] Curtis N. Wiens, Shawn J. Kisch, Jacob D. Willig-Onwuachi, and Charles A. McKenzie. Computationally rapid method of estimating signal-to-noise ratio for phased array image reconstructions. *Magn. Reson. Med.*, 66(4):1192–1197, 2011. doi: 10.1002/mrm.22893.
- [32] Onat Dalmaz, Arjun D Desai, Reinhard Heckel, Tolga Cukur, Akshay S Chaudhari, and Brian Hargreaves. Efficient noise calculation in deep learning-based MRI reconstructions. In Aarti Singh, Maryam Fazel, Daniel Hsu, Simon Lacoste-Julien, Felix Berkenkamp, Tegan Maharaj, Kiri Wagstaff, and Jerry Zhu, editors, *Proceedings of the 42nd International Conference on Machine Learning*, volume 267 of *Proceedings of Machine Learning Research*, pages 12280–12313. PMLR, 13–19 Jul 2025. URL <https://proceedings.mlr.press/v267/dalmaz25a.html>.
- [33] P. Dawood, F. Breuer, M. Gram, I. Homolya, P. M. Jakob, M. Zaiss, and M. Blaimer. Image space formalism of convolutional neural networks for k-space interpolation. *Magnetic Resonance in Medicine*, 94(6):2680–2701, 2025. doi: <https://doi.org/10.1002/mrm.70002>. URL <https://onlinelibrary.wiley.com/doi/abs/10.1002/mrm.70002>.
- [34] Istvan Homolya, Jannik Stebani, Felix Breuer, Grit Hein, Matthias Gamer, Florian Knoll, and Martin Blaimer. Controlling spatial correlation in k-space interpolation networks for MRI reconstruction: denoising versus apparent blurring. *arXiv preprint arXiv:2505.11155*, 2025. doi: 10.48550/arXiv.2505.11155.
- [35] Michael F. Hutchinson. A stochastic estimator of the trace of the influence matrix for laplacian smoothing splines. *J. Commun. Statist. Simula.*, 19(2):433–450, 1990. URL <https://cir.nii.ac.jp/crid/1573668925763299072>.
- [36] C. Bekas, E. Kokiopoulou, and Y. Saad. An estimator for the diagonal of a matrix. *Applied Numerical Mathematics*, 57(11):1214–1229, 2007. ISSN 0168-9274. doi: <https://doi.org/10.1016/j.apnum.2007.01.003>. URL <https://www.sciencedirect.com/science/article/pii/S0168927407000244>. Numerical Algorithms, Parallelism and Applications (2).
- [37] Michael S. Hansen and Peter Kellman. Image reconstruction: an overview for clinicians. *J. Magn. Reson. Imaging*, 41(3):573–585, 2015. doi: 10.1002/jmri.24687.
- [38] Kylie Yeung, Christine Tobler, Rolf F Schulte, Benjamin White, Anthony McIntyre, Sébastien Serres, Peter Morris, Dorothee Auer, Fergus V Gleeson, Damian J Tyler, et al. Algebraic

- methods and computational strategies for pseudoinverse-based mr image reconstruction (pinv-recon). *Scientific Reports*, 15(1):37997, 2025.
- [39] Michael Lustig, David L. Donoho, Juan M. Santos, and John M. Pauly. Compressed sensing mri. *IEEE Signal Processing Magazine*, 25(2):72–82, 2008. doi: 10.1109/MSP.2007.914728.
- [40] Kevin Epperson, Anne Marie Sawyer, Michael Lustig, Marcus Alley, Martin Uecker, Patrick Virtue, Peng Lai, and Shreyas Vasanaawala. Creation of fully sampled mr data repository for compressed sensing of the knee. ISMRM 2013 Meeting Proceedings. Section for Magnetic Resonance Technologists, 2013.
- [41] Leslie Ying and Jinhua Sheng. Joint image reconstruction and sensitivity estimation in sense (jsense). *Magnetic Resonance in Medicine*, 57:1196–1202, 2007. ISSN 15222594. doi: 10.1002/mrm.21245.
- [42] Martin Uecker, Peng Lai, Mark J. Murphy, Patrick Virtue, Michael Elad, John M. Pauly, Shreyas S. Vasanaawala, and Michael Lustig. Espirit - an eigenvalue approach to autocalibrating parallel mri: Where sense meets grappa. *Magnetic Resonance in Medicine*, 71:990–1001, 2014. ISSN 15222594. doi: 10.1002/mrm.24751.
- [43] Florian Knoll, Jure Zbontar, Anuroop Sriram, Matthew J. Muckley, Mary Bruno, Aaron Defazio, Marc Parente, Krzysztof J. Geras, Joe Katsnelson, Hersh Chandarana, Zizhao Zhang, Michal Drozdal, Adriana Romero, Michael Rabbat, Pascal Vincent, James Pinkerton, Duo Wang, Nafissa Yakubova, Erich Owens, C. Lawrence Zitnick, Michael P. Recht, Daniel K. Sodickson, and Yvonne W. Lui. fastmri: A publicly available raw k-space and dicom dataset of knee images for accelerated mr image reconstruction using machine learning. *Radiology: Artificial Intelligence*, 2(1):e190007, 2020. doi: 10.1148/ryai.2020190007. URL <https://doi.org/10.1148/ryai.2020190007>. PMID: 32076662.
- [44] Amir Beck and Marc Teboulle. A fast iterative shrinkage-thresholding algorithm for linear inverse problems. *SIAM Journal on Imaging Sciences*, 2(1):183–202, 2009. doi: 10.1137/080716542.
- [45] Florian Knoll, Kristian Bredies, Thomas Pock, and Rudolf Stollberger. Second order total generalized variation (tgv) for mri. *Magnetic Resonance in Medicine*, 65(2):480–491, 2011. doi: <https://doi.org/10.1002/mrm.22595>. URL <https://onlinelibrary.wiley.com/doi/abs/10.1002/mrm.22595>.
- [46] Adam Paszke, Sam Gross, Francisco Massa, Adam Lerer, James Bradbury, Gregory Chanan, Trevor Killeen, Zeming Lin, Natalia Gimelshein, Luca Antiga, Alban Desmaison, Andreas Köpf, Edward Yang, Zach DeVito, Martin Raison, Alykhan Tejani, Sasank Chilamkurthy, Benoit Steiner, Lu Fang, Junjie Bai, and Soumith Chintala. *PyTorch: an imperative style, high-performance deep learning library*. Curran Associates Inc., Red Hook, NY, USA, 2019.
- [47] Frank Ong and Michael Lustig. Sigpy: A python package for high performance iterative reconstruction. *Proc. Intl. Soc. Mag. Reson. Med.*, 27:4819, 2019.
- [48] R.W. Brown, Y.C.N. Cheng, E.M. Haacke, M.R. Thompson, and R. Venkatesan. *Magnetic Resonance Imaging: Physical Principles and Sequence Design*. Wiley, 2014. ISBN 9781118633977. URL <https://books.google.com/books?id=rQGCawAAQBAJ>.
- [49] Catherine Westbrook, Carolyn Kaut Roth, and John Talbot. *MRI in Practice*. Wiley-Blackwell, 5th edition, 2018. ISBN 978-1119391968.

- [50] Haim Avron and Sivan Toledo. Randomized algorithms for estimating the trace of an implicit symmetric positive semi-definite matrix. *Journal of the ACM*, 58(2):8, 2011. doi: 10.1145/1944345.1944349.
- [51] Philip M. Robson, Aaron K. Grant, Ananth J. Madhuranthakam, Riccardo Lattanzi, Daniel K. Sodickson, and Charles A. McKenzie. Comprehensive quantification of signal-to-noise ratio and g-factor for image-based and k-space-based parallel imaging reconstructions. *Magnetic Resonance in Medicine*, 60(4):895–907, 2008. doi: 10.1002/mrm.21728.
- [52] Florian Knoll, Kerstin Hammernik, Chi Zhang, Steen Moeller, Thomas Pock, Daniel K. Sodickson, and Mehmet Akcakaya. Deep-learning methods for parallel magnetic resonance imaging reconstruction: a survey of the current approaches, trends, and issues. *IEEE Signal Process. Mag.*, 37(1):128–140, 2020. doi: 10.1109/MSP.2019.2950640.
- [53] Matti Hanhela, Mikael Delić, Aku Nissinen, and Ville Kolehmainen. Data-driven regularization parameter selection in dynamic MRI. *J. Imaging*, 7(2):38, 2021. doi: 10.3390/jimaging7020038.
- [54] Mathieu Boudreau, Agah Karakuzu, Julien Cohen-Adad, Ecem Bozkurt, Madeline Carr, Marco Castellaro, Luis Concha, Mariya Doneva, Seraina A. Dual, Alex Ensworth, Alexandru Foias, Véronique Fortier, Refaat E. Gabr, Guillaume Gilbert, Carri K. Glide-Hurst, Matthew Grech-Sollars, Siyuan Hu, Oscar Jalnefjord, Jorge Jovicich, Kübra Keskin, Peter Koken, Anastasia Kolokotronis, Simran Kukran, Nam G. Lee, Ives R. Levesque, Bochao Li, Dan Ma, Burkhard Mädler, Nyasha G. Maforo, Jamie Near, Erick Pasaye, Alonso Ramirez-Manzanares, Ben Statton, Christian Stehning, Stefano Tambalo, Ye Tian, Chenyang Wang, Kilian Weiss, Niloufar Zakariaei, Shuo Zhang, Ziwei Zhao, Nikola Stikov, and the ISMRM Reproducible Research Study Group and the ISMRM Quantitative MR Study Group . Repeat it without me: Crowdsourcing the t1 mapping common ground via the ismrn reproducibility challenge. *Magnetic Resonance in Medicine*, 92(3):1115–1127, 2024. doi: <https://doi.org/10.1002/mrm.30111>. URL <https://onlinelibrary.wiley.com/doi/abs/10.1002/mrm.30111>.
- [55] Siria Pasini, Steffen Ringgaard, Tau Vendelboe, Leyre Garcia-Ruiz, Anika Strittmatter, Giulia Villa, Anish Raj, Rebeca Echeverria-Chasco, Michela Bozzetto, Paolo Brambilla, Malene Aastrup, Esben S. S. Hansen, Luisa Pierotti, Matteo Renzulli, Susan T. Francis, Frank G. Zöllner, Christoffer Laustsen, Maria A. Fernandez-Seara, and Anna Caroli. Multi-center and multi-vendor evaluation study across 1.5 T and 3 T scanners (part 2): T1 and T2 standardization in the ISMRM/NIST MR phantom. *Magnetic Resonance Materials in Physics, Biology and Medicine*, 38(3):611–627, July 2025. doi: 10.1007/s10334-025-01260-4. URL <https://doi.org/10.1007/s10334-025-01260-4>.
- [56] Eros Montin, Xuan Thao Nguyen, and Riccardo Lattanzi. MR Optimum: A web-based open-source tool for standardized signal-to-noise ratio evaluation in MRI. *Computer Methods and Programs in Biomedicine Update*, page 100235, 2026. doi: 10.1016/j.cmpbup.2026.100235.
- [57] Jeremiah J. Hess, Catherine J. Moran, Preya Shah, Jana Vincent, Fraser J. L. Robb, Bruce L. Daniel, and Brian A. Hargreaves. Relative SNR measurements in supine vs. prone breast MRI. *Magnetic Resonance in Medicine*, 95(5):2718–2725, 2026. doi: 10.1002/mrm.70217.
- [58] Gaël Varoquaux, Flore Baronnet, Andreas Kleinschmidt, Pierre Fillard, and Bertrand Thirion. Detection of brain functional-connectivity difference in post-stroke patients using group-level covariance modeling. In Tianzi Jiang, Nassir Navab, Josien P. W. Pluim, and Max A. Viergever,

- editors, *Medical Image Computing and Computer-Assisted Intervention – MICCAI 2010*, pages 200–208, Berlin, Heidelberg, 2010. Springer Berlin Heidelberg. ISBN 978-3-642-15705-9.
- [59] Ali Behrouz, Parsa Delavari, and Farnoosh Hashemi. Unsupervised representation learning of brain activity via bridging voxel activity and functional connectivity. In *Proceedings of the 41st International Conference on Machine Learning (ICML)*, volume 235 of *Proceedings of Machine Learning Research*, pages 3347–3381, 2024.
- [60] Brian Toner. Methods for uncertainty quantification in dictionary matching to advance interpretable quantitative MRI. Sedona, AZ, United States of America, January 2026. Proc. Intl. Soc. Mag. Reson. Med. Workshop on Data Sampling and Image Reconstruction. URL <https://echo.ismrm.org/program/SEDONA26>. Abstract #00187.
- [61] Vandana V. Hanchate and Kalyani R. Joshi. Mri denoising using bm3d equipped with noise invalidation denoising technique and vst for improved contrast. *SN Applied Sciences*, 2(2):234, 2020.
- [62] Zhoubo Li, Lifeng Yu, Joshua D. Trzasko, David S. Lake, Daniel J. Blezek, Joel G. Fletcher, Cynthia H. McCollough, and Armando Manduca. Adaptive nonlocal means filtering based on local noise level for ct denoising. *Medical Physics*, 41(1):011908, 2014. doi: 10.1118/1.4851635.
- [63] Sai Gokul Hariharan, Norbert Strobel, Christian Kaethner, Markus Kowarschik, Rebecca Fahrig, and Nassir Navab. Data-driven estimation of noise variance stabilization parameters for low-dose x-ray images. *Physics in Medicine and Biology*, 65(22):225027, 2020. doi: 10.1088/1361-6560/abbc82.
- [64] Yongjian Yu and Scott T. Acton. Speckle reducing anisotropic diffusion. *IEEE Transactions on Image Processing*, 11(11):1260–1270, 2002. doi: 10.1109/TIP.2002.804276.
- [65] Quan Dou, Zhixing Wang, Xue Feng, Adrienne E. Campbell-Washburn, John P. Mugler, and Craig H. Meyer. Mri denoising with a non-blind deep complex-valued convolutional neural network. *NMR in Biomedicine*, 38(1):e5291, 2025. doi: 10.1002/nbm.5291.
- [66] Xin Wang, Xiaoyu Liu, Peng Huang, Pu Huang, Shu Hu, and Hongtu Zhu. U-medsam: Uncertainty-aware medsam for medical image segmentation. In Jun Ma, Yuyin Zhou, and Bo Wang, editors, *Medical Image Segmentation Foundation Models. CVPR 2024 Challenge: Segment Anything in Medical Images on Laptop*, pages 206–217, Cham, 2025. Springer Nature Switzerland. ISBN 978-3-031-81854-7.
- [67] Hui Xue, Sarah M. Hooper, Iain Pierce, Rhodri H. Davies, John Stairs, Joseph Naegele, Adrienne E. Campbell-Washburn, Charlotte Manisty, James C. Moon, Thomas A. Treibel, Michael S. Hansen, and Peter Kellman. SNRAware: Improved deep learning MRI denoising with signal-to-noise ratio unit training and g-factor map augmentation. *Radiology: Artificial Intelligence*, 7(6):e250227, 2025. doi: 10.1148/ryai.250227.
- [68] Hui Xue, Sarah Hooper, Azaan Rehman, Iain Pierce, Thomas Treibel, Rhodri Davies, W. Patricia Bandettini, Rajiv Ramasawmy, Ahsan Javed, Zheren Zhu, Yang Yang, James Moon, Adrienne Campbell, and Peter Kellman. Imaging transformer for MRI denoising with the SNR unit training: enabling generalization across field-strengths, imaging contrasts, and anatomy, 2024. arXiv:2404.02382.

- [69] Klaas P. Pruessmann, Markus Weiger, Markus B. Scheidegger, and Peter Boesiger. Sense: Sensitivity encoding for fast mri. *Magnetic Resonance in Medicine*, 42(5):952–962, 1999. doi: 10.1002/(SICI)1522-2594(199911)42:5<952::AID-MRM16>3.0.CO;2-S.
- [70] Harrison H. Barrett. Task-based measures of image quality and their relation to radiation dose and patient risk. *Physics in Medicine and Biology*, 60(2):R1–R75, 2015. doi: 10.1088/0031-9155/60/2/R1.
- [71] Sergey Kastruyulin, Jamil Zakirov, Nicola Pezzotti, and Dmitry V. Dylov. Image quality assessment for magnetic resonance imaging. *IEEE Access*, 11:14154–14168, 2023. doi: 10.1109/ACCESS.2023.3243466.
- [72] Yueran Ma, Jianxun Lou, Jean-Yves Tanguy, Pdraig Corcoran, and Hantao Liu. Rad-IQMRI: A benchmark for MRI image quality assessment. *Neurocomputing*, 602:128292, 2024. doi: 10.1016/j.neucom.2024.128292.
- [73] Chenwei Tang, Laura B. Eisenmenger, Leonardo Rivera-Rivera, Eugene Huo, Jacqueline C. Junn, Anthony D. Kuner, Thekla H. Oechtering, Anthony Peret, Jitka Starekova, and Kevin M. Johnson. Incorporating radiologist knowledge into MRI quality metrics for machine learning using rank-based ratings. *Journal of Magnetic Resonance Imaging*, 61(6):2572–2584, 2025. doi: 10.1002/jmri.29672.
- [74] Roman Vershynin. *High-Dimensional Probability: An Introduction with Applications in Data Science*. Cambridge Series in Statistical and Probabilistic Mathematics. Cambridge University Press, Cambridge, 2 edition, 2026.

Algorithm 1 Probing Image-space COvariance (PICO)

Require: Encoding operator \mathbf{A} (and adjoint \mathbf{A}^H); regularization parameter $\lambda \geq 0$; number of probes N ; image dimension N_x .

Ensure: Estimated voxelwise noise variance map $\hat{\sigma}_{\hat{\mathbf{x}}}^2 \approx \text{diag}(\Sigma_{\hat{\mathbf{x}}})$.

```
1:  $\mathbf{s} \leftarrow \mathbf{0} \in \mathbb{C}^{N_x}$  ▷ Running sum across probes
2: for  $i = 1$  to  $N$  do
3: ▷ (1) Draw a unit-magnitude random-phase probe
4:    $\theta_k \sim \text{Uniform}[0, 2\pi]$  for  $k = 1, \dots, N_x$ 
5:    $v_k^{(i)} \leftarrow e^{j\theta_k}$  for  $k = 1, \dots, N_x$ 
6: ▷ (2, 3) Apply  $\Sigma_{\hat{\mathbf{x}}}$  implicitly via CG
7:    $\mathbf{u}^{(i)} \leftarrow \Sigma_{\hat{\mathbf{x}}} \mathbf{v}^{(i)}$  via CG on the normal equations
8: ▷ (4) Accumulate elementwise product
9:    $\mathbf{s} \leftarrow \mathbf{s} + \mathbf{v}^{(i)*} \odot \mathbf{u}^{(i)}$ 
10: end for
11:  $\hat{\sigma}_{\hat{\mathbf{x}}}^2 \leftarrow \text{Re}(\mathbf{s}/N)$  ▷ Imaginary part vanishes in expectation
```

Supporting Information

A PICO Algorithm Pseudocode

Algorithm 1 summarizes the PICO procedure as implemented in all experiments reported in the main text. The algorithm is stated for the linear case, where the covariance operator $\Sigma_{\hat{\mathbf{x}}} = \mathbf{R}\mathbf{R}^H$ is applied implicitly via forward/adjoint primitives and a CG solve on the normal equations. For nonlinear reconstructions, the covariance–vector product $\Sigma_{\hat{\mathbf{x}}}\mathbf{v}^{(i)}$ in line 7 is replaced by a Jacobian–vector product $\mathbf{J}_f(\mathbf{k}_0)\mathbf{v}^{(i)}$ evaluated via automatic differentiation at the converged reconstruction (Sec. 2.2.5); the remainder of the algorithm is unchanged.

Each probe response in line 7 is obtained by applying $\Sigma_{\hat{\mathbf{x}}} = \mathbf{R}\mathbf{R}^H$ implicitly through the same forward/adjoint primitives (\mathbf{A} , \mathbf{A}^H , FFT/NUFFT, Toeplitz embedding, coil sensitivity maps) and CG solver already present in the CG-SENSE reconstruction pipeline. The reconstruction operator \mathbf{R} and the covariance matrix $\Sigma_{\hat{\mathbf{x}}}$ are never formed explicitly. Computational cost is dominated by the per-probe CG work in line 7, which reuses the same inner solver as CG-SENSE reconstruction.

B Variance of the Stochastic Diagonal Estimator

Let $\Sigma_{\hat{\mathbf{x}}} = \mathbf{R}\mathbf{R}^H \in \mathbb{C}^{N_x \times N_x}$ be positive-semidefinite (and necessarily Hermitian by construction), and define for a single probe image $\mathbf{v} \in \mathbb{C}^{N_x}$ with i.i.d. entries satisfying $\mathbb{E}[v_k] = 0$, $\mathbb{E}[|v_k|^2] = 1$, and $\mathbb{E}[v_k^* v_\ell] = 0$ for $k \neq \ell$, the voxelwise point estimator

$$\delta_k(\mathbf{v}) = v_k^* (\Sigma_{\hat{\mathbf{x}}} \mathbf{v})_k, \quad k = 1, \dots, N_x.$$

Because $\mathbb{E}[v_k^* v_\ell] = \delta_{k\ell}$, the estimator is unbiased: $\mathbb{E}[\delta_k(\mathbf{v})] = (\Sigma_{\hat{\mathbf{x}}})_{kk}$.

Single-sample variance. Let $\kappa := \mathbb{E}[|v_k|^4]$ denote the fourth moment of the probe distribution. Expanding $(\Sigma_{\hat{\mathbf{x}}}\mathbf{v})_k = (\Sigma_{\hat{\mathbf{x}}})_{kk}v_k + \sum_{\ell \neq k} (\Sigma_{\hat{\mathbf{x}}})_{k\ell}v_\ell$ and using independence yields

$$\text{Var}[\delta_k(\mathbf{v})] = (\kappa - 1) |(\Sigma_{\hat{\mathbf{x}}})_{kk}|^2 + \sum_{\ell \neq k} |(\Sigma_{\hat{\mathbf{x}}})_{k\ell}|^2. \quad (\text{A1})$$

The per-sample variance separates into two contributions: a *diagonal-dependent term* $(\kappa - 1)|(\boldsymbol{\Sigma}_{\hat{\mathbf{x}}})_{kk}|^2$ that is controlled by the kurtosis κ of the probe distribution and scales with the squared local noise variance, and an *off-diagonal interference term* $\sum_{\ell \neq k} |(\boldsymbol{\Sigma}_{\hat{\mathbf{x}}})_{k\ell}|^2$ that is invariant across probe distributions and depends only on the noise leakage from neighboring voxels into voxel k . Minimizing the per-sample variance subject to the unit-variance constraint $\mathbb{E}[|v_k|^2] = 1$ therefore reduces to minimizing κ , which determines the choice of probe distribution analyzed below.

Choice of probe distribution. Three distributions satisfying the probe conditions are compared:

- *Complex Gaussian probes* ($v_k \sim \mathcal{CN}(0, 1)$) yield $\kappa = 2$, contributing one unit of the diagonal squared magnitude to the per-sample variance for every probe.
- *Real ± 1 Rademacher probes* ($v_k \in \{-1, +1\}$ with $\mathbb{P}(v_k = +1) = \mathbb{P}(v_k = -1) = 1/2$) attain $\kappa = 1$, eliminating the diagonal-dependent contribution. Since $\kappa \geq 1$ for any unit-variance distribution (by Jensen’s inequality), this is the kurtosis-optimal real-valued choice.
- *Unit-magnitude random-phase probes* ($v_k = e^{i\theta_k}$, $\theta_k \sim \mathbf{U}[0, 2\pi]$, so that $|v_k| = 1$ deterministically while only the phase varies across draws) also attain $\kappa = 1$, matching the kurtosis of real Rademacher probes. Unlike real Rademacher, however, each unit-magnitude random-phase sample carries two real degrees of freedom—the sine and cosine of a uniformly distributed phase—which permits the estimator to interact with the imaginary components of the off-diagonal entries $(\boldsymbol{\Sigma}_{\hat{\mathbf{x}}})_{k\ell}$. For the complex Hermitian covariances arising in MRI reconstruction, this doubles the information extracted per sample relative to real Rademacher and halves the number of probes required to reach a given target accuracy.

Proposition (Optimal probe distribution). Under the constraints $\mathbb{E}[\mathbf{v}] = \mathbf{0}$ and $\mathbb{E}[\mathbf{v}\mathbf{v}^H] = \mathbf{I}$, unit-magnitude random-phase probes minimize the per-sample variance $\text{Var}[\delta_k(\mathbf{v})]$ in (A1) for complex Hermitian positive-semidefinite $\boldsymbol{\Sigma}_{\hat{\mathbf{x}}}$, and are therefore optimal for the proposed stochastic diagonal estimator.

C Theoretical Error Bounds and Convergence Rates

We analyze the concentration properties of the two estimators using standard inequalities for sums of independent random variables [74].

C.1 PMR: sub-exponential concentration

The PMR estimator $\hat{\sigma}_{\text{PMR}}^2$ is the sample variance of N complex-Gaussian reconstruction outputs. The squared magnitude of each output follows an exponential distribution, so the sum follows a Gamma distribution with sub-exponential tails. Applying the Bernstein inequality for sums of independent sub-exponential random variables [74, Theorem 2.8.1] yields

$$\mathbb{P}\left(|\hat{\sigma}_{\text{PMR}}^2 - \sigma_k^2| \geq t\right) \leq 2 \exp\left(-cN \min\left(\frac{t^2}{(\sigma_k^2)^2}, \frac{t}{\sigma_k^2}\right)\right). \quad (22)$$

The decay rate is controlled by $(\sigma_k^2)^2$: as acceleration increases, local noise variance σ_k^2 grows via the g -factor, and the probability of large deviations increases quadratically. PMR is therefore disproportionately unstable in high- g -factor regions.

C.2 PICO: sub-Gaussian concentration

PICO uses unit-magnitude random-phase probes with $|v_k| = 1$ deterministically. The diagonal-dependent contribution to the single-sample variance (Eq. (A1)) vanishes because the kurtosis term $(\kappa - 1)$ is zero; estimation error arises solely from off-diagonal interference. Since the real and imaginary parts of each probe component are bounded on $[-1, 1]$, the per-voxel estimator $\delta_k(\mathbf{v})$ is a sum of bounded random variables, and Hoeffding's inequality [74, Theorem 2.2.5] applied to the real and imaginary parts gives

$$\mathbb{P}\left(|\hat{\sigma}_{\text{Prop}}^2 - \sigma_k^2| \geq t\right) \leq 2 \exp\left(-\frac{2 N t^2}{\sum_{j \neq k} |(\boldsymbol{\Sigma}_{\hat{\mathbf{x}}})_{kj}|^2}\right). \quad (23)$$

The bound depends on the off-diagonal energy (noise leakage) but is independent of the diagonal variance σ_k^2 itself. At low acceleration, the covariance is nearly diagonal and the denominator is small, yielding rapid convergence. At high acceleration, off-diagonal energy increases, but the estimator does not incur the $(\sigma_k^2)^2$ penalty of PMR, and the sub-Gaussian decay ($\exp(-t^2)$) ensures tighter concentration than the sub-exponential tails characteristic of PMR. This confirms a fundamental stability advantage: PICO decouples estimation precision from the local noise level.

D Variance Shrinkage under Tikhonov Regularization

We work in the pre-whitened setting of Sec. 2, where $\mathbf{b}_w = \mathbf{A}\mathbf{x} + \mathbf{n}_w$ with $\mathbf{n}_w \sim \mathcal{CN}(\mathbf{0}, \mathbf{I})$. Let $\mathbf{M} := \mathbf{A}^H \mathbf{A} \succeq \mathbf{0}$.

Proposition 1 (Modewise variance shrinkage). *Assume \mathbf{M} is positive-definite, and fix $\lambda > 0$. The unregularized least-squares and Tikhonov reconstruction operators*

$$\mathbf{R}_{\text{LS}} = (\mathbf{A}^H \mathbf{A})^{-1} \mathbf{A}^H, \quad \mathbf{R}_\lambda = (\mathbf{A}^H \mathbf{A} + \lambda \mathbf{I})^{-1} \mathbf{A}^H$$

have image-domain noise covariances

$$\boldsymbol{\Sigma}_{\hat{\mathbf{x}}, \text{LS}} = \mathbf{M}^{-1}, \quad \boldsymbol{\Sigma}_{\hat{\mathbf{x}}, \lambda} = (\mathbf{M} + \lambda \mathbf{I})^{-1} \mathbf{M} (\mathbf{M} + \lambda \mathbf{I})^{-1}.$$

Then $\boldsymbol{\Sigma}_{\hat{\mathbf{x}}, \lambda} \prec \boldsymbol{\Sigma}_{\hat{\mathbf{x}}, \text{LS}}$ in the Loewner order for every $\lambda > 0$, and consequently $\text{diag}(\boldsymbol{\Sigma}_{\hat{\mathbf{x}}, \lambda}) < \text{diag}(\boldsymbol{\Sigma}_{\hat{\mathbf{x}}, \text{LS}})$ elementwise.

Proof. Let $\mathbf{M} = \mathbf{U} \boldsymbol{\Lambda} \mathbf{U}^H$ with eigenvalues $\lambda_i > 0$. Define $\mathbf{X} := \mathbf{M}^{1/2} (\mathbf{M} + \lambda \mathbf{I})^{-1} \mathbf{M}^{1/2} = \mathbf{U} \text{diag}\left(\frac{\lambda_i}{\lambda_i + \lambda}\right) \mathbf{U}^H$. Then $\boldsymbol{\Sigma}_{\hat{\mathbf{x}}, \lambda} = \mathbf{M}^{-1/2} \mathbf{X}^2 \mathbf{M}^{-1/2}$ and $\boldsymbol{\Sigma}_{\hat{\mathbf{x}}, \text{LS}} = \mathbf{M}^{-1/2} \mathbf{I} \mathbf{M}^{-1/2}$. Since $0 < \frac{\lambda_i}{\lambda_i + \lambda} < 1$ for all $\lambda_i > 0$, we have $\mathbf{0} \prec \mathbf{X}^2 \prec \mathbf{I}$. Congruence with $\mathbf{M}^{-1/2}$ preserves the order, giving the result. \square

Corollary 1 (Regularization can yield $g < 1$). *With $g(i) = \sigma_{\hat{\mathbf{x}}, \text{acc}, \lambda}(i) / (\sqrt{R} \sigma_{\hat{\mathbf{x}}, \text{ref}}(i))$, classical unregularized SENSE implies $g \geq 1$. Tikhonov regularization introduces shrinkage factors $(\lambda_j / (\lambda_j + \lambda))^2 < 1$ along each singular mode j . Where this shrinkage outweighs the geometric noise inflation from undersampling, $g(i) < 1$ is observed.*

Remarks. (i) Under non-white acquisition noise, all statements hold after pre-whitening with $\mathbf{A} = \mathbf{L}^{-1} \tilde{\mathbf{A}}$ and $\mathbf{n}_w = \mathbf{L}^{-1} \mathbf{n}$, where $\mathbf{L} \mathbf{L}^H = \boldsymbol{\Sigma}_{\mathbf{n}}$. (ii) If \mathbf{M} is rank-deficient, the inequalities are strict on its positive spectrum; nullspace components do not affect voxel variances within the range of \mathbf{A}^H .

E PMR Convergence Protocol and Reference Budgets

For settings without a closed-form noise model, surrogate reference variance maps were defined by high-replica PMR [27]. To certify convergence of the reference, the following protocol was applied: (1) compute a gold-standard PMR map at N_{\max} replicas; (2) evaluate voxelwise NRMSE and the change in ROI-mean variance (ΔROI) at each intermediate N relative to the gold map; (3) declare convergence at the smallest N such that doubling the replica count improves NRMSE by $< 0.5\%$ and ΔROI by $< 0.2\%$.

Non-Cartesian spiral physical phantom. For the prospectively acquired non-Cartesian spiral brain phantom (a physical phantom imaged on a GE 3T scanner; see Sec. 3.1), the gold map was computed at $N_{\max} = 50,000$ replicas (4,340 s). The reference used in the main-text experiments was set at $N_{\text{ref}} = 30,000$ replicas (2,604 s), at which point the NRMSE relative to the gold was $\approx 0.4\%$ —well below 1% —and $\Delta\text{ROI} \approx 0.001\%$. Increasing the replica count from N_{ref} to N_{\max} produced negligible further improvement, confirming that the $N_{\text{ref}} = 30,000$ reference is adequately converged for the 1% NRMSE operating points reported in the main text.

Nonlinear TV-regularized compressed sensing. Because PICO’s Jacobian-based approximation and PMR converge to slightly different asymptotic limits in the nonlinear regime (the former to the first-order Jacobian covariance, the latter to the true nonlinear variance), a single shared reference is not appropriate. Method-specific gold maps were instead computed at $N_{\max} = 50,000$ (1,614 s) for both the proposed Jacobian-based estimator and PMR. Convergence was reached at $N_{\text{ref}} = 5,000$ (NRMSE $\approx 1.5\%$, $\Delta\text{ROI} \approx 0.1\%$; wall-clock 161.4 s). Doubling to $N = 10,000$ reduced NRMSE to $\approx 1.2\%$, an improvement of $< 0.5\%$, confirming adequate convergence at N_{ref} .

These converged reference maps define the baselines against which NRMSE is evaluated in the main text. Because each method is assessed against its own converged limit, the reported NRMSE curves reflect internal convergence rates rather than absolute accuracy differences between estimators.